

WIND TUNNEL TESTING OF LOAD-ALLEVIATING MEMBRANE WINGS

By

YAAKOV JACK ABUDARAM

A THESIS PRESENTED TO THE GRADUATE SCHOOL  
OF THE UNIVERSITY OF FLORIDA IN PARTIAL FULFILLMENT  
OF THE REQUIREMENTS FOR THE DEGREE OF  
MASTER OF SCIENCE

UNIVERSITY OF FLORIDA

2009

© 2009 Yaakov Jack Abudaram

To my mother, who has given me her unconditional love, and has shown me the way to success.

## ACKNOWLEDGMENTS

The most special thanks to Dr. Peter Ifju for being a great advisor by giving the best possible and practical solutions to the most challenging problems I have encountered during the time I had spent at the MAV lab, and, of course, for funding me throughout the entire time I spent in the graduate school. His intelligence level is proportionate to his compassion toward people, which makes him an exceptional being. Those who work for him are the most fortunate students, and he is an ideal boss everybody would wish for.

Thanks go out to Kyuho Lee for teaching me the skills to manufacture airplanes, being a good friend and a supervisor at the same time, and also trying to teach me how to fly. I learned it from the best, and without him this thesis would not have been possible.

I owe my deepest gratitude to Dr. Bret Stanford, who taught me the most fundamental and important concepts about the flexible wings. He is the one who suggested the hot topics that I am presenting in this thesis, and he is the mastermind behind most of the ideas covered in this work. He has answered every single email I sent and every question I asked promptly, diligently, and patiently to the full extent.

Thanks go out to Dr. Rick Lind and Dr. David Jenkins for accepting to be in my committee. I also would like to thank Albert Lin and Vijay Jagdale for helping me a great deal in visual image correlation testing and post-processing.

Thanks go out to my future wife, Eda, for feeding me while I was spending extensive hours at the wind tunnel; consequently, keeping my mind fresh to keep the tunnel running. She has also been a wonderful emotional help in writing my thesis. It is said every successful man has a woman behind him. The woman behind me has been my mother; therefore, I thank her from the bottom of my heart for being a great support in my life.

## TABLE OF CONTENTS

	<u>page</u>
ACKNOWLEDGMENTS .....	4
LIST OF TABLES .....	6
LIST OF FIGURES .....	7
NOMENCLATURE .....	10
ABSTRACT.....	11
CHAPTER	
1 INTRODUCTION .....	12
2 EXPERIMENTAL TECHNIQUES.....	16
2.1 Wind Tunnel .....	16
2.2 Sting Balance.....	17
2.3 Visual Image Correlation.....	18
2.4 Membrane Wings.....	20
2.4.1 Latex Membrane Wing.....	20
2.4.2 Crinkled Silicone Membrane Wing.....	21
3 RESULTS.....	25
3.1 Latex Membrane Batten Reinforced Wing Results .....	25
3.1.1 Effect of Reynolds Number.....	27
3.1.2 Effect of Batten Stiffness.....	33
3.1.3 Spanwise Stiffness Gradient.....	38
3.1.4 Batten Spacing and Trailing Edge Shape .....	41
3.2 Silicone Perimeter Reinforced Membrane Wing Results.....	42
3.2.1 Crinkled Silicone Membrane Specimen .....	44
3.2.1.1 Visual image correlation (VIC) testing.....	45
3.2.1.2 Aerodynamic load testing.....	51
3.2.2 Test for Surface Effects .....	54
3.2.3 Test for Geometrical Effects .....	55
4 CONCLUSIONS AND FUTURE WORK .....	57
APPENDIX EXTRA VISUAL IMAGE CORELATION IMAGES.....	59
LIST OF REFERENCES.....	60
BIOGRAPHICAL SKETCH .....	62

## LIST OF TABLES

<u>Table</u>		<u>page</u>
3-1	The relationship between angle of attack ( $\alpha$ ), crinkle angle ( $\theta$ ), and the highest deformation value experienced by the membrane (w).....	46

## LIST OF FIGURES

<u>Figure</u>	<u>page</u>
2-1 Closed loop wind tunnel with the large test section installed. ....	16
2-2 Sting balance mounted on model arm. ....	18
2-3 Schematic of the wind tunnel setup. ....	20
2-4 Load-alleviating membrane wing. ....	21
2-5 Aluminum and epoxy molds for silicon rubber. ....	22
2-6 Steps to fabricate the crinkled silicone membrane for the wing. ....	23
2-7 Four parts of the wing that will be assembled together. ....	24
2-8 Fully assembled crinkled silicone membrane wing. ....	24
3-1 Load alleviating membrane wing. ....	25
3-2 Wing structure definitions. ....	26
3-3 Wing deformation parameters of interest: wing twisting ( $\alpha$ ), cambering ( $z$ ), and bending ( $\delta$ ). ....	27
3-4 Chord normalized out-of-plane displacement ( $w/c$ ) along semi-wing of wing1 $\alpha=10^\circ$ ...	28
3-5 Spanwise strain ( $\epsilon_{yy}$ ) along the semi-wing of wing 1, $\alpha = 10^\circ$ . ....	28
3-6 Local angle of attack along the semi-wing of wing 1 at 7 m/s (left) and 12 m/s (right). ....	30
3-7 Local maximum camber along the semi-wing of wing 1 at 7 m/s (left) and 12 m/s (right). ....	31
3-8 Local bending along the semi-wing of wing at 7 m/s (left) and 12 m/s (right). ....	32
3-9 Lift coefficients of wing 1: angle of attack is measured at the rigid root. ....	33
3-10 Chord -normalized deformed semi-wing shape ( $z/c$ ), $\alpha = 10^\circ$ . ....	35
3-11 Local angle of attack along the semi-wing at 7 m/s (left) and 12 m/s (right), $\alpha = 10^\circ$ . ...	35
3-12 Local maximum camber along the semiwing at 7 m/s (left) and 12 m/s (right), $\alpha=10^\circ$ ...	36
3-13 Local bending along the semi-wing at 7 m/s (left) and 12 m/s (right), $\alpha = 10^\circ$ . ....	37

3-14	Lift coefficients: angle of attack is measured at the rigid root.....	38
3-15	Local angle of attack along the semi-wing at 7 m/s (left) and 12 m/s (right), $\alpha = 10^\circ$ ...	39
3-16	Local maximum camber along the semi-wing at 7 m/s (left) and 12 m/s (right), $\alpha = 10^\circ$ .....	39
3-17	Local bending along the semi-wing at 7 m/s (left) and 12 m/s (right), $\alpha = 10^\circ$ .....	40
3-18	Lift coefficients: angle of attack is measured at the rigid root.....	41
3-19	Lift coefficients: angle of attack is measured at the rigid root.....	42
3-20	Specimens sandwiched in the wing apparatus.....	43
3-21	Crinkle angle notation for both the silicone membrane wing and the silicone membrane with a rigid carbon-fiber plate beneath.....	44
3-22	Elliptical silicone membrane wing and notation for showing the angle of the ellipse. ...	44
3-23	Uniaxial stretch test with the crinkle pattern normal to, and parallel to, the loading. ....	45
3-24	Deformation on the left side of the wing at $\theta=0^\circ$ and $\alpha=10^\circ$ .....	47
3-25	Deformation on the left side of the wing at $\theta=0^\circ$ and $\alpha=15^\circ$ .....	47
3-26	Deformation on the left side of the wing at $\theta=45^\circ$ and $\alpha=10^\circ$ .....	48
3-27	Deformation on the left side of the wing at $\theta=45^\circ$ and $\alpha=15^\circ$ .....	48
3-28	Deformation on the left side of the wing at $\theta=90^\circ$ and $\alpha=10^\circ$ .....	49
3-29	Deformation on the left side of the wing at $\theta=90^\circ$ and $\alpha=15^\circ$ .....	49
3-30	Deformation on the left side of the wing at $\theta=135^\circ$ and $\alpha=10^\circ$ .....	50
3-31	Deformation on the left side of the wing at $\theta=135^\circ$ and $\alpha=15^\circ$ .....	50
3-32	Lift curves of four different crinkle angles and rigid wing at 15 m/s. ....	51
3-33	Lift over drag curves of all tested angles of specimen and rigid wing at 15 m/s.....	52
3-34	Pitching moment slope for crinkled membrane versus crinkle angle at 15 m/s. ....	53
3-35	Lift over drag ratio versus crinkle angle at $\alpha=6^\circ$ and 15 m/s.....	53
3-36	Lift over drag ratio curve tested at 15 m/s for four different crinkle angles with the specimen shown in 3-20B. ....	55

A-1	Deformation on the left side of the wing at $\theta=105^\circ$ and $\alpha=10^\circ$ .....	59
A-2	Deformation on the left side of the wing at $\theta=105^\circ$ and $\alpha=15^\circ$ .....	59

## NOMENCLATURE

$\alpha$	angle of attack
$b$	wing span
$c$	chord
$C_L$	lift coefficient
$C_{L\alpha}$	lift curve slope
$\varepsilon_{yy}$	spanwise strains
$N$	image correlation grid spacing
$Re$	Reynolds number
$u, v, w$	Cartesian displacements
$U_\infty$	free-stream velocity
$x, y, z$	Cartesian coordinates
$\delta$	leading edge displacement
$\theta$	crinkle angle
$\gamma$	ellipse minor axis angle

Abstract of Thesis Presented to the Graduate School  
of the University of Florida in Partial Fulfillment of the  
Requirements for the Master of Science

WIND TUNNEL TESTING OF LOAD-ALLEVIATING MEMBRANE WINGS

By

Yaakov Jack Abudaram

December 2009

Chair: Peter Ifju

Major: Mechanical Engineering

This work is concerned with wind tunnel testing of elastic latex and silicone membrane wings intended for micro air vehicles. Erratic flow conditions are a particular problem for the smooth controllability of such vehicles, and so stiff batten structures are imbedded into the trailing edge of the membrane wing, intended to passively washout under aerodynamic loading. Several disparate wing structures are fabricated, with varying batten thicknesses and spacing.

Another wing with an anisotropic membrane skin is fabricated mimicking the wing skins of biological flyers, such as bats and pterosaurs. In this work an artificial anisotropic membrane skin was utilized on a wing with different orientations to observe and analyze various deformations and loadings in the wind tunnel at low Reynolds Numbers. These passive deformations are not always effective however, particularly at higher angles of attack or higher speeds and so this work is intended to provide some understanding of the complex role of wing structure and flight speed upon aerodynamic performance of membrane wings.

Data, in terms of measured aerodynamic loads and structural deformation, is given for a wide range of relatively low Reynolds numbers. Drastic changes in lift slopes, stalling conditions and deformation patterns are found for certain combinations of flight speed and wing structure.

## CHAPTER 1 INTRODUCTION

The controllability and range of operation of small micro air vehicles (MAVs) can be greatly diminished in the presence of unsteady, gusty conditions. Indoor flight (envisioned for very small flapping vehicles) may suffer from similar problems, due to air vents and ducting, for example. While several complex, active mechanisms may be envisioned to maintain smooth level flight in unsteady conditions [1], the energy budgets onboard MAVs are limited [2], and simple passive mechanisms may suffice. Extremely compliant wings have been used for MAV platforms [1], where the wing structure is predicated by some combination of carbon fiber composites (wing skeleton), and a latex rubber membrane skin, sealed to the suction side of the aforementioned skeleton. The wing topology can be tailored to obtain the desired change in aerodynamic performance through passive shape adaptation [4].

Load-alleviation is of obvious interest here (through, for example, unsteady gust alleviation, delayed stall, shallow lift-alpha slopes, minimized drag, etc.), and may be obtained with a very flexible trailing edge. The trailing edge deflects upwards due to aerodynamic loading, resulting in a nose-down geometric twist of the flexible wing section. This adaptive washout decreases the wing's disturbance to the flow field, and thus the loads. For example, as the vehicle hits a head-on wind gust the overall airspeed suddenly increases. The larger dynamic pressure causes the wing to twist and decrease the lifting efficiency. Because the airspeed is higher however, the wing maintains a near-constant lift history: the result is a wing that flies with exceptional smoothness, even in gusty conditions.

However, such a relationship between dynamic pressure and elastic wing compliance may not always be so straightforward. Increasing the flight speed accentuates the positive deflection of the trailing edge described above for load alleviation, but alters the Reynolds number as well.

Reynolds numbers for typical fixed wing micro air vehicles are between  $10^4$  and  $10^5$ , a span that sees extremely complex and mutable flow fields develop over a wing [5]: flow separation, transition, and reattachment [6], periodic vortex shedding, swirling, and pairing [7], and strong interactions with three-dimensional tip vortices [8] have all been reported. The underlying physics, as discussed by Young and Horton [9], depend on many factors including Reynolds number and wing shape, the latter of which is not pre-determined for an elastic membrane wing.

Though many suitable aeroelastic computational tools exist [3] for membrane micro air vehicle wings, they cannot always be expected to faithfully reproduce the complex physics described above, particularly in post-stall regimes. Experimental wind tunnel testing can provide an initial link between wing structure, Reynolds number, and load alleviation, which can in turn be used to tune the aeroelastic models for a detailed exploration of the design space. Existing literature on wind tunnel testing of membrane wings generally discuss up to three facets of the underlying physics: loads measurements (lift, drag, etc.), shape measurements (displacements and strains of the elastic membrane under aerodynamic loading), and flow measurements.

Shape measurements for membrane wings are typically non-contact optical methods, as strain gages and load cells are too intrusive. Song et al. [10] use stereo photogrammetry for displacement measurements of a membrane sheet stretched between two rigid posts, with a reported resolution between 35 and 40  $\mu\text{m}$ . Data is available at discrete markers placed along the wing. Projection moiré interferometry requires no such marker placement (a fringe pattern is projected onto the wing surface), and the resulting data set is full-field. However, displacement resolutions reported by Fleming et al. [11] for micro air vehicle work are relatively poor (250  $\mu\text{m}$ ), the dual-camera system must be rotated during the  $\alpha$ -sweep, and only out-of-plane data is available, making strain calculations (if needed) impossible. Stanford et al. [3] utilize a visual

image correlation system for membrane wings, which is a full-field speckle-based technique with a displacement resolution of 10  $\mu\text{m}$ . This method is utilized in the current work as well, and will be described below. Wu et al. [12] have extended the image correlation method for high speed deformation measurements of flapping membrane wings.

Experimental flow measurements for membrane wings include recent work with particle image velocimetry (PIV) by Hu et al. [13] and Rojratsirikul et al. [14] concerning an aspect ratio-5 membrane wing. The former is able to show that trailing edge washout can keep the flow attached to the flexible surface up to  $14^\circ$  angle of attack, while a rigid wing under similar conditions shows a very large separation bubble. The latter find that mean membrane shape is insensitive to angle of attack, though time-averaged flow is not, through the development of flow separation and vortex shedding. The authors are also able to show a strong time-dependent correlation between membrane vibration and the height of the shear layer [14]. A similar wing is studied by Mastramico and Hubner [15] to correlate the elastic membrane structure with the velocity deficits within the wake.

The current work is concerned with experimentally establishing a general relationship between shape deformation measurements and load measurements of load-alleviating membrane wings, for a variety of wing structures, Reynolds numbers, and angles of attack. When possible, results will be further compared to existing flow measurement data in the literature. The outline of the current work is as follows: a general description of the experimental setup will be given, in terms of the wind tunnel facility, sting balance, and image correlation system. A description of the array of wing structures used for testing is discussed, followed by the first part of results: cambering, twist, wing bending, in-plane strains, and lift coefficients are given for a variety of cases. Second part of results elaborates the images that were provided by the VIC system, then

shows a relationship between crinkle angle, lift, drag, lift over drag, pitching moment, and finally analyzes the effects of surface and different orientations of geometrical effects. Load-alleviating wings generally present a trade-off in aerodynamic performance: the compliant nature of the wing allows for gust rejection, delayed stall, etc, but the lift in steady flight typically degrades as well, diminishing the payload capacity and the minimum cruise speed. The ability of a wing structure to decrease the lift slope or delay the onset of stall, as compared to a nominally rigid model, is of particular interest.

## CHAPTER 2 EXPERIMENTAL TECHNIQUES

### 2.1 Wind Tunnel

Experimental testing is facilitated by wing deformation and flight load measurements, both conducted within a wind tunnel. The test facility used for the entirety of this work is an Engineering Laboratory Design 407B closed loop wind tunnel, with the flow loop arranged in a horizontal configuration. The test section has an inner dimension of 0.84 m on each side, and is 2.44 m long (Figure 2-1). Also, the section has glass side walls and ceiling for observation of the model and visual imaging, which will be explained in detail in Section 2.3. The velocity range is between 2 and 45 m/s (maximum Re of 2.7 million), provided by a 250 HP motor and a 2-stage axial fan. Centerline turbulence levels have been measured on the order of 0.2%. Optical access is available on the sidewalls and the ceiling. A Heise model PM differential pressure transducer is attached to a pitot-static tube located at the center of the section's entrance, while a four-wire RTD mounted to the wall of the test section measures the airflow temperature.



Figure 2-1. Closed loop wind tunnel with the large test section installed.

## 2.2 Sting Balance

An Aerolab 01-15 6-component strain gage sting balance is used to measure the aerodynamic forces and moments of the wind tunnel models. Each of the six channels is in a full Wheatstone-bridge configuration, with 5 channels dedicated to force, and 1 to a moment. Data acquisition is done with a NI SCXI 1520 8 channel programmable strain gage module with full bridge configuration, 2.5 excitation volts, and a gain of 1000. A NI 6052 DAQ PAD firewire provides A/D conversion, multiplexing, and the PC connection. For a given flight condition, the output signals from the six components are sampled at 1000 Hz for 2 seconds. The average of this data is sent to a LabVIEW-based module for the calculation of the relevant aerodynamic coefficients, and the standard deviation of the data is stored for an uncertainty analysis.

Corrections are applied to the aerodynamic coefficients to account for blockage (solid, wake and streamline curvature) and flexibility effects. The latter is chiefly caused by the wind tunnel model's slightly flexible support (strain gage sting balance). Wind loads cause the model to pitch up in the wind tunnel. Visual image correlation (described below) is used to measure the small rigid body movement in order to correct the angle of attack. The sting balance is mounted to a custom-fabricated aluminum model arm within the test section (Figure 2-2). The arm extends through a hole in the section wall, and is then attached to a gearbox and a brushless servomotor system for angle of attack control (rates on the order of 1 °/s). Tunnel speed, model inclination, and force/moment measurements are set/acquired using a dedicated PC and in-house LabVIEW-based software.

The drag data that was gotten from sting balance for wings that have larger spans was seen to be bogus, in which this result may be caused by the 3-D effects since the tips are too close to the walls of the test section. However, for shorter spans, like the one that is shown in Figure 3-21, the drag coefficients converged to result logical values.



Figure 2-2. Sting balance mounted on model arm.

### **2.3 Visual Image Correlation**

Wing deformation is measured with visual image correlation (VIC), a non-contacting full-field measurement technique originally developed by researchers at the University of South Carolina. The underlying principle is to calculate the displacement field of a test specimen by tracking the deformation of a random speckling pattern applied to the surface [16]. Two pre-calibrated cameras digitally acquire this pattern before and after loading, using stereo-triangulation techniques. The VIC system then tries to find a region (in the image of the deformed specimen) that maximizes a normalized cross-correlation function corresponding to a small subset of the reference image (taken when no load is applied to the structure). The image space is iteratively swept by the parameters of the cross-correlation function to transform the coordinates of the original reference frame to coordinates within the deformed image. As it is unlikely that the deformed coordinates will directly fall onto the sampling grid of the reference image, accurate grey-value interpolation schemes are implemented to achieve optimal sub-pixel accuracy without bias [17].

In order to capture the three-dimensional features and deformation of a wind tunnel model, twin synchronized cameras, each looking from a different viewing angle, are installed above the wind tunnel ceiling. As the cameras must remain stationary throughout the experiment, a mounting bracket straddles the tunnel to prevent the transmission of vibration. Optical access into the test section is through a glass ceiling. Two continuous 250 W lamps illuminate the model, enabling the use of exposure times of 5 to 10 ms. The energy emitted from the lights, a potential hazard for the specimen (particularly the thin membrane skin, whose elastic properties are known to degrade in adverse conditions), was not a concern due to the cooling effect of the wind tunnel flow. A schematic of the final wind tunnel setup can be seen in Figure 2-3.

The twin cameras are connected with a PC via an IEEE 1394 firewire cable, and a specialized unit is used to synchronize the camera triggers for instantaneous shots. A standard acquisition board installed in the computer carries out digitalization of the images, and the image processing is carried out by custom software, provided by Correlated Solutions, Inc. Typical data results obtained from the VIC system consist of geometry of the surface in discrete coordinates  $(x, y, z)$  and the corresponding displacements  $(u, v, w)$ . The VIC system places a grid point every  $N$  pixels, where  $N$  is user defined. A final post-processing option involves calculating the in-plane strains  $(\epsilon_{xx}, \epsilon_{yy}, \text{ and } \epsilon_{xy})$ . This is done by mapping the displacement field onto an unstructured triangular mesh, and conducting the appropriate numerical differentiation (the complete definition of finite strains is used).

The general procedural steps used in this work are:

- 1) Take a picture of the wind tunnel model at the set angle of attack, with the wind off.
- 2) Start the wind tunnel, and wait for stable conditions.
- 3) Take a picture of the deformed wing, and record the aerodynamic loads.
- 4) Stop the wind tunnel, move the model to the next angle, and repeat.

Each pair of images is then sent to the VIC system for processing. The acquired displacement field is composed of both the elastic deformation of the wing and the rigid body motions inherent within the wind tunnel setup. These motions are thought to primarily originate from the flexibility of the sting balance, and must be filtered out. The computed strain field is, theoretically, unaffected by these motions.

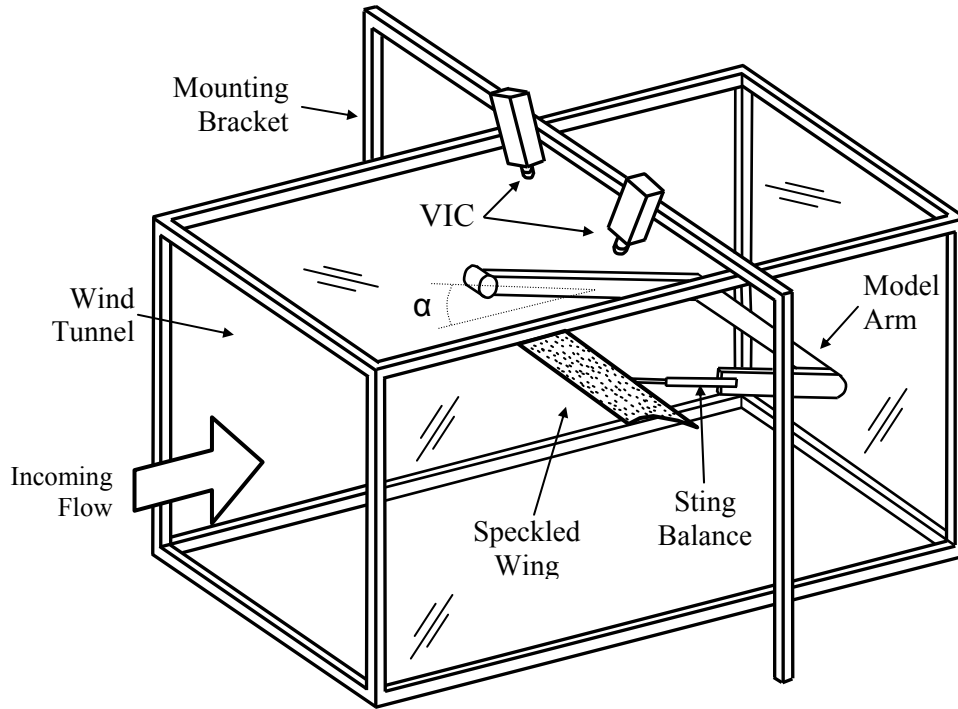


Figure 2-3. Schematic of the wind tunnel setup.

## 2.4 Membrane Wings

### 2.4.1 Latex Membrane Wing

The latex membrane wing under consideration for this work can be seen in Figure 2-4. It is a rectangular wing, with a 10 cm chord and a 4.8 aspect ratio. The maximum camber is 3.2% (at  $x/c = 0.3$ ). The wing is built up from a “T” at the leading edge and root, constructed from four layers of bi-directional plain-weave graphite/epoxy. Ten battens (strips of uni-directional carbon fiber) extend from the leading edge to the trailing edge of each semi-wing. A thin latex rubber skin (0.1 mm thick) is glued to the suction side of this carbon fiber skeleton. The battens

can potentially be excluded for enhanced flexibility, but the membrane skin alone is prone to excessive vibration above a critical dynamic pressure [18], resulting in a severe drag penalty. The procedures outlined by Albertani et al. [19] are used to facilitate visual image correlation testing. The carbon fiber skeleton is painted white, a random black speckle pattern is applied to the translucent latex membrane, and the skin is then affixed to the skeleton with a spray adhesive. The result presents a nearly-homogenous image for the VIC cameras, which should be unable to discern the location of the skeleton beneath the speckle pattern.

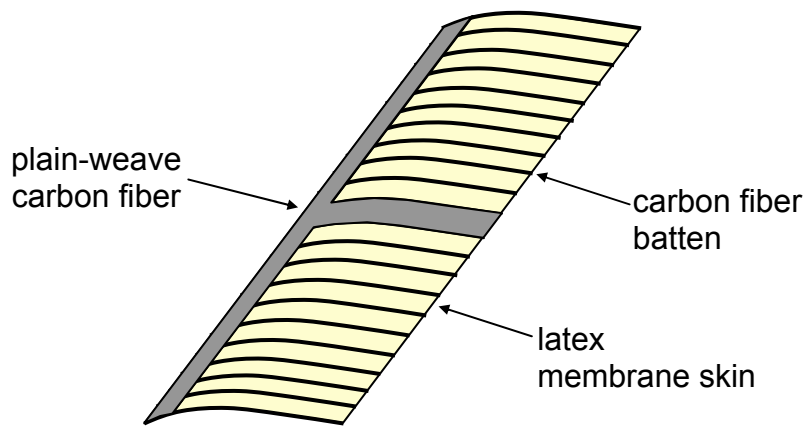


Figure 2-4. Load-alleviating membrane wing.

#### 2.4.2 Crinkled Silicone Membrane Wing

The crinkled silicone membrane wing is a rectangular wing with a 10cm chord and 2.0 aspect ratio (Figure 2-8). The maximum camber is same as the latex membrane wing since the same mold was used to manufacture the wing. Two rigid parts were constructed from four layers of bi-directional plain-weave graphite/epoxy; afterward, a hole of 73mm was carved out on each side of the upper and lower parts of the wing symmetrically and simultaneously to ensure the same geometry for both parts. To fabricate the crinkled silicone membrane an aluminum mold is manufactured by milling with a fly-wheel creating equally spaced grooves. Another mold is formed by pouring epoxy on the top of the aluminum mold to create an identical match for the other side of the silicone rubber as seen in Figure 2-5.

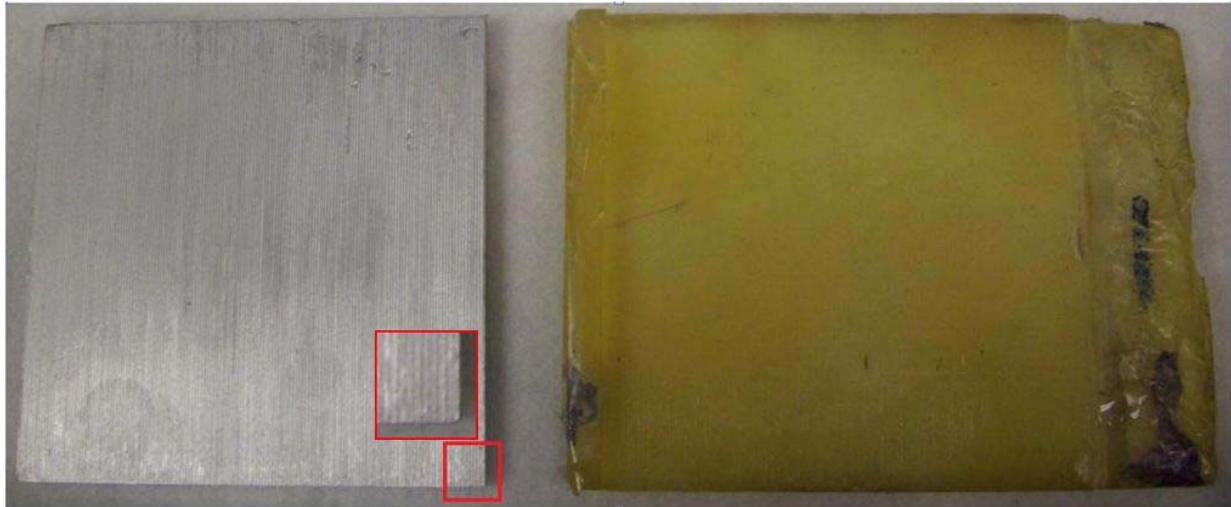


Figure 2-5. Aluminum and epoxy molds for silicon rubber.

Following steps are applied for the fabrication of the crinkled silicone membrane:

- 1) Two parts of silicone rubber are mixed thoroughly.
- 2) The mixture is transferred into the two test tubes to be put in the centrifuge machine to remove the entrapped air bubbles.
- 3) The liquid silicone is pooled onto the surface corner of the epoxy mold that was applied a thin release film previously to make the de-bonding process easier.
- 4) Aluminum mold is started to be pressed from the corner at an angle and pushed down until the desired thickness is achieved, which is dictated by a thin indenter [27].
- 5) After the silicone is cured, the molds are separated for the final product to be used (Figure 2-5).

The crinkled silicone membrane has a wavelength of 0.8mm, amplitude of 0.17mm, and thickness of 0.1mm [26]. Finalized crinkled silicone membrane is speckled for visual image correlation test and glued onto a carbon-fiber ring with zero tension (Figure 2-7). Four small holes were drilled around each one of the 73mm holes to keep the entire structure intact with screws. Button-head screws were used for a more aerodynamic design. Finally, the apparatus was sandwiched between the upper and lower surfaces of the wing at the desired crinkle angle (Figure 2-8). Whenever the crinkle angle wanted to be adjusted, the screws were loosened and the specimens were rotated to the new desired angle. This angle was measured with a digital inclinometer that is sensitive to 0.1°.

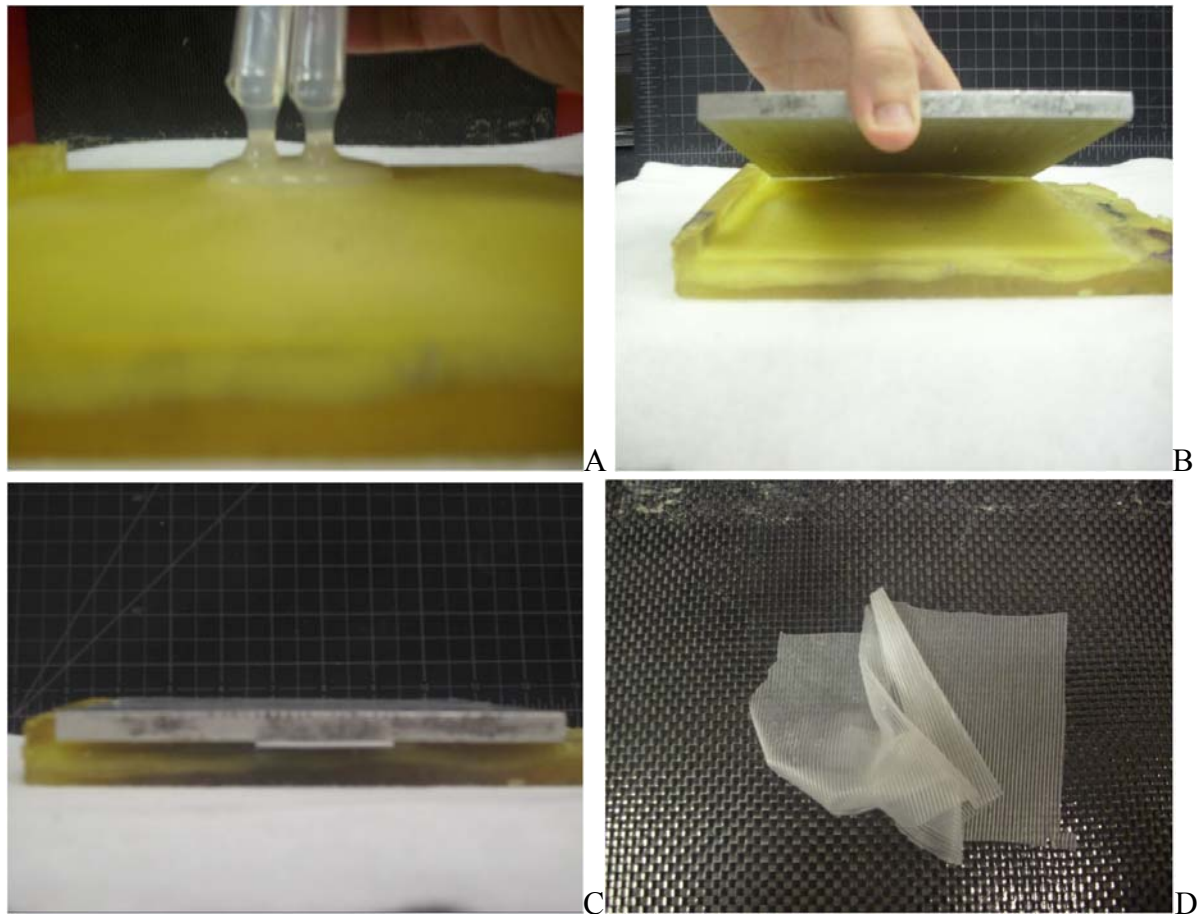


Figure 2-6. Steps to fabricate the crinkled silicone membrane for the wing. A) pouring the liquid silicone at the corner of the epoxy mold, B) pushing down the aluminum mold by slowly decreasing the angle between the two molds, C) pressing the aluminum mold to squeeze out the excess silicone with two indenters in the middle, D) finalized fabrication of the crinkled silicone membrane.

The fabrication was initially done by utilizing five clamps at various locations of the two pieces of molds that had the liquid silicone in between; however, because the pressure was not exactly the same at each clamp, uniform thickness was not achieved. Another manufacturing process was tried by sandwiching the liquid silicone between the molds under hydrostatic pressure by placing the entire assembly into the vacuum bag, which theoretically would yield a membrane that would have a constant value of thickness along each direction. However, vacuuming caused air bubbles inside the membrane.

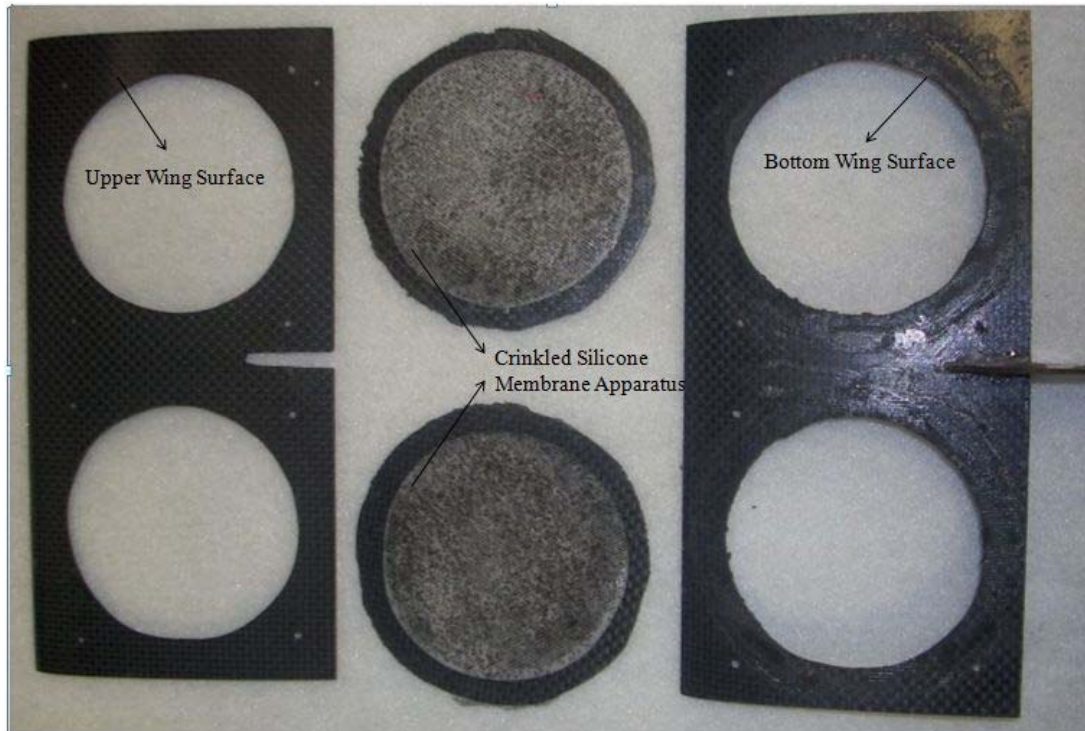


Figure 2-7. Four parts of the wing that will be assembled together.

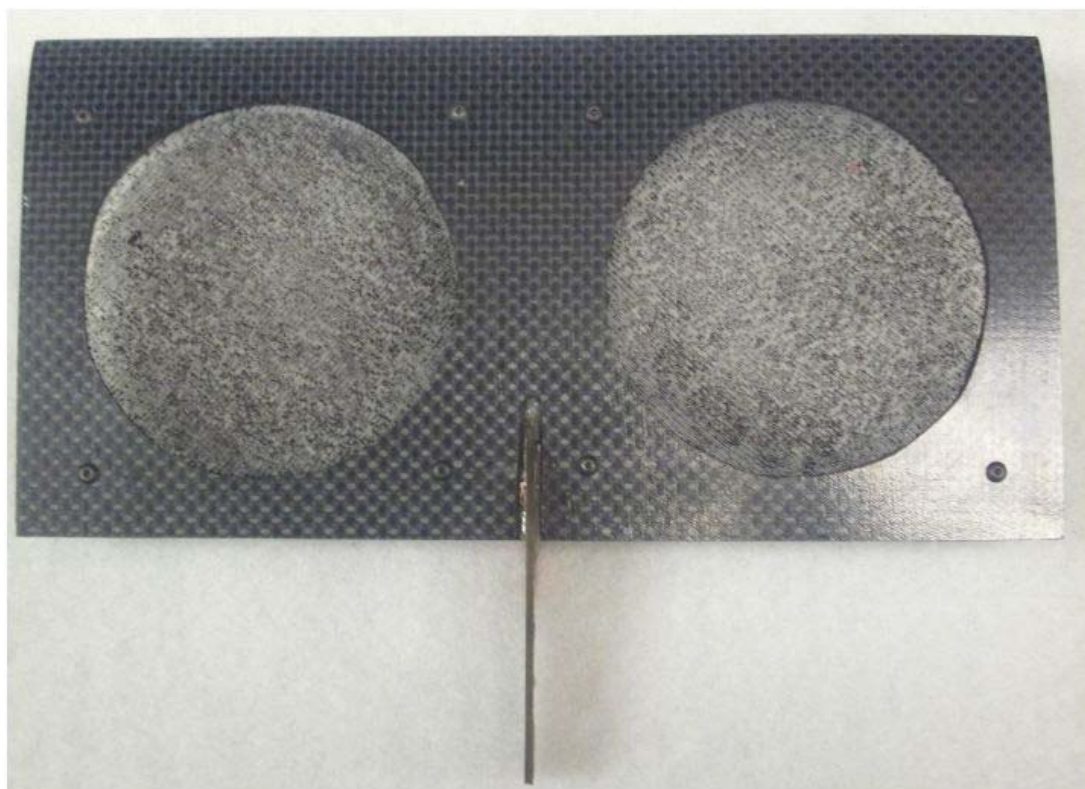


Figure 2-8. Fully assembled crinkled silicone membrane wing.

## CHAPTER 3 RESULTS

### 3.1 Latex Membrane Batten Reinforced Wing Results

This work seeks to elucidate the relationship between lift, lift slope, and stall behavior of a membrane wing through wind tunnel testing. While the number of relevant design variables for this problem is large (including planform shape, ply layup schedule of the plain-weave, pre-tension within the membrane skin, among others), only two are considered in this work: flight speed and batten thickness. Flight speed (through the Reynolds number) directly impacts the behavior of the flow structures, and (through the dynamic pressure) impacts the deformation of the structure as well. The battens are allowed to have between 1 and 4 layers of carbon fiber each, or can be removed entirely. The carbon fiber “T” is fixed at four layers of plain-weave oriented at  $45^\circ$  to the flow, and the membrane skin is slack for the entirety of the experiments. The resulting array of experiments is of course very large (5 design variables for each of the ten battens, and wind speed is allowed to vary between 5 and 15 m/s in increments of 2 m/s), and so a select number of interesting cases are presented for membrane wing characterization.

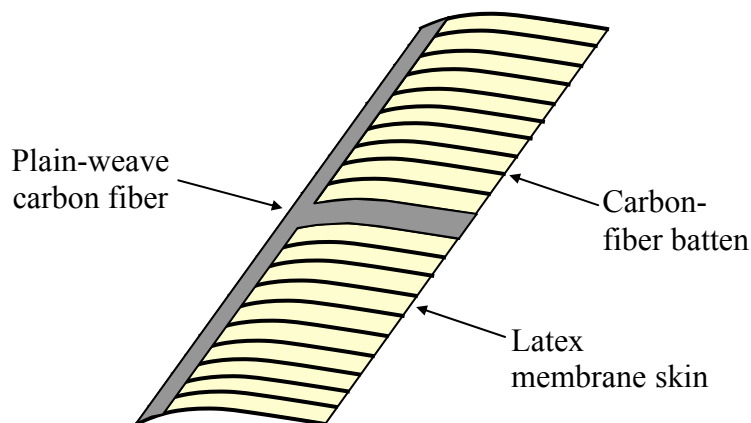


Figure 3-1. Load alleviating membrane wing.

The array of wing structures considered in this work is defined in Figure 3-2. The numbers beneath each wing denote the number of layers of carbon fiber used to construct each batten.

Only the semi-wing is shown, though of course each wing will be built symmetrically. Wing 1 utilizes single-layer battens throughout the structure, while wings 2-4 simply increase the thickness of each batten, uniformly throughout the wing. Wings 5, 6, and 7 explore the effect of adding a spanwise stiffness gradient to the wing, by either tailoring stiffness gradually toward the root (wing 5) or toward the wingtip (gradually with wing 6, or suddenly with wing 7 which has a very stiff outer batten). Finally, wings 8 and 9 will provide information on the effect of batten spacing, with every other batten removed from the membrane structure. As the large amount of un-reinforced membrane is expected to vibrate along the trailing edge (and detrimentally affect the aerodynamic performance), a scalloped trailing edge is introduced in wing 9 to potentially offset this behavior.

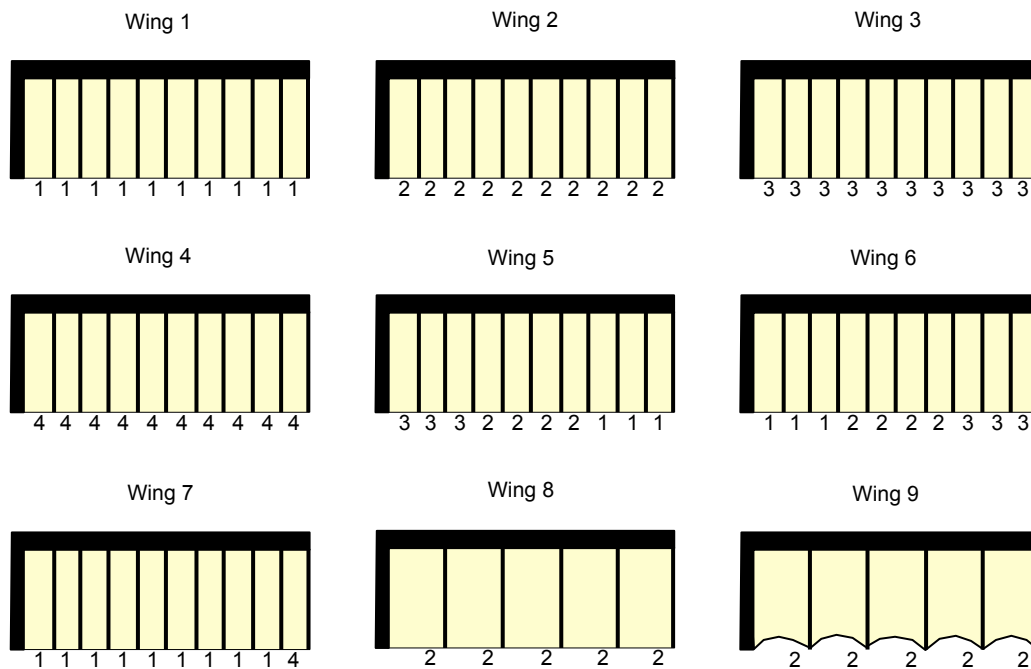


Figure 3-2. Wing structure definitions.

The visual image correlation system is capable of providing full-field data along the wing, as discussed above, but comparisons between disparate wing structures is occasionally enhanced by compressing the data into three parameters of interest. Assuming that the spanwise motion of

each wing section is negligible compared to chordwise and transverse movements, these parameters are given in Figure 3-3. Wing twist is quantified by the local angle of attack, measured with respect to the free-stream velocity. The maximum camber of each flexible wing section is reported, as well as the transverse displacement of the leading edge. All three metrics can be measured as a function of the spanwise position along the wing.

### 3.1.1 Effect of Reynolds Number

The range of tested flight speeds (5 to 15 m/s) equates to fairly low chord-based Reynolds numbers between  $3.3 \cdot 10^4$  and  $10^5$ . The flow structures present throughout this range of Reynolds numbers should show substantial variations, and thus aerodynamic performance will as well. As reviewed by Carmichael [20]: for Reynolds numbers below  $5 \cdot 10^4$ , the laminar separated flow may not have time to reattach to the surface. Above  $5 \cdot 10^4$ , the flow may reattach, forming a long separation bubble over the wing. For increased Reynolds numbers, the size of the bubble decreases, generally resulting in a decrease in form drag.

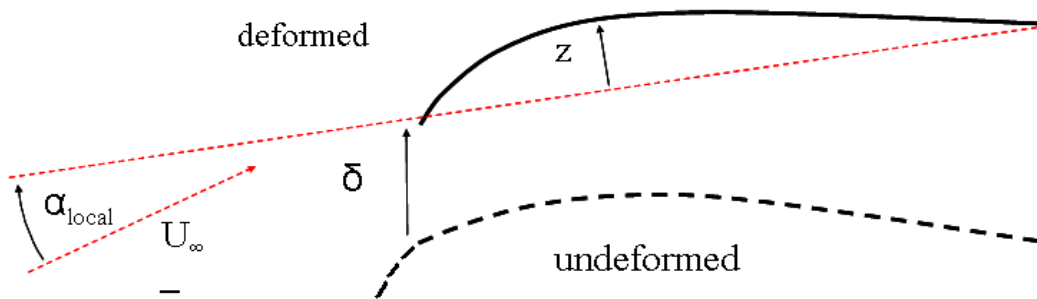


Figure 3-3. Wing deformation parameters of interest: wing twisting ( $\alpha$ ), cambering ( $z$ ), and bending ( $\delta$ ).

Results in this section are given solely in terms of wing 1, tested between 5 and 15 m/s in increments of 2 m/s as discussed above. An  $\alpha$ -sweep between  $0^\circ$  and  $40^\circ$  in increments of  $1^\circ$  is conducted for each speed, and aerodynamic loads are measured for each case. Elastic

deformation is measured at select pre-stall conditions. Deformation is sampled at 1 Hz for 10 seconds, and loads are sampled at 1000 Hz for 2 seconds. The chord-normalized out-of-plane displacements and spanwise strains that develop over the semi-wing of wing 1 can be seen in Figure 3-4 and Figure 3-5, at  $10^\circ$  angle of attack and both 7 m/s and 12 m/s. The deformation at the root is close to zero (as this portion of the wing is attached to the wind tunnel sting balance, as seen in Figure 2-3), and each subsequent flexible wing section sees a substantial trailing edge washout, upwards of 30% of the root chord.

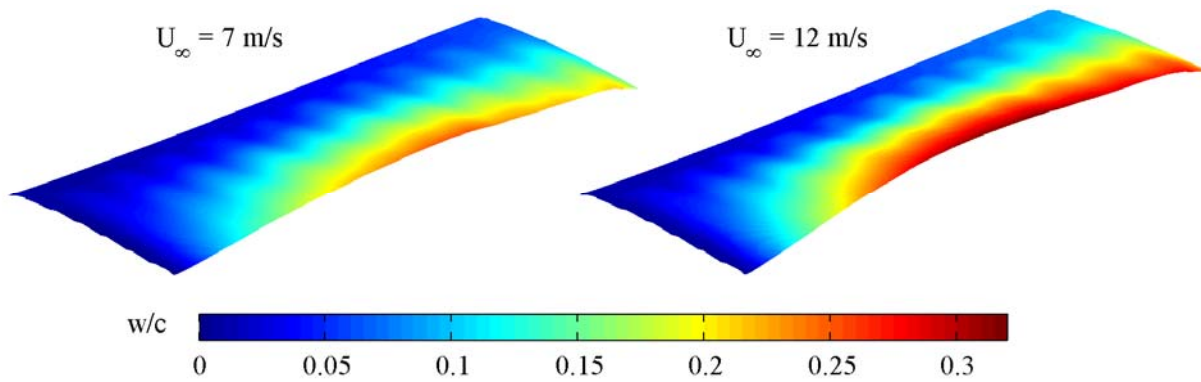


Figure 3-4. Chord normalized out-of-plane displacement ( $w/c$ ) along semi-wing of wing1  $\alpha=10^\circ$ .

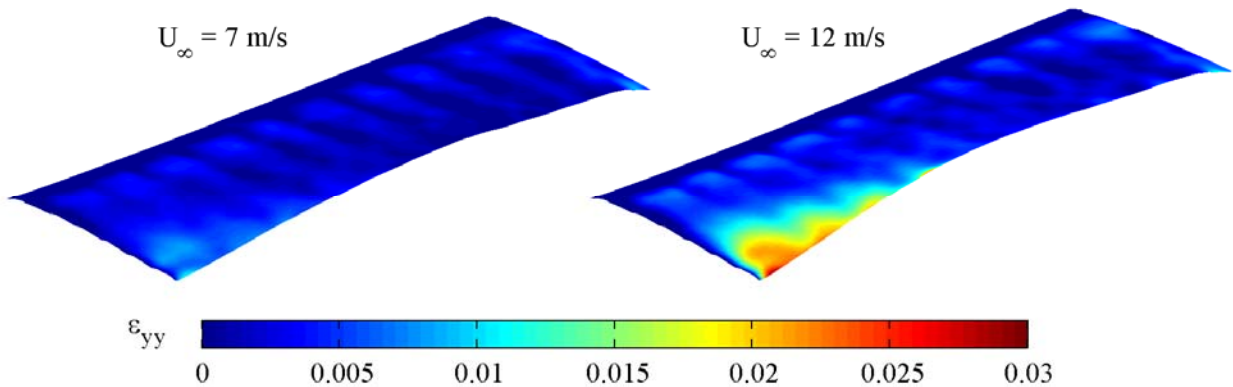


Figure 3-5. Spanwise strain ( $\epsilon_{yy}$ ) along the semi-wing of wing 1,  $\alpha = 10^\circ$ .

The resolution of the VIC system (estimated at  $10 \mu\text{m}$  for displacements) is evident from Figure 3-4, as the carbon fiber areas of the wing (battens) can be clearly differentiated from the membrane skin. Aside from the nose-down twist of each flexible wing section, the membrane

portions of the wing show a local inflation toward the leading edge, and an overall wing bending deformation pattern is visible as well. The majority of the deformation is located toward the center of the semi-wing; this is a result of the loading pattern. Although the structure is weakest at the wing tip (due to a uniformly distributed load, for example), the sectional lift is estimated to be largest at the root and decrease to zero at the wing tip (from simple lifting line theorems [21], for example). For higher speeds (12 m/s in Figure 3-4) substantial twisting is seen at the tip as well.

Only the spanwise strain is reported here (Figure 3-5), as the battens prevent appreciable chordwise stretching [3]. The strain resolution of the VIC system is estimated to be  $500 \mu\epsilon$ , a relatively high value (compared to strain gages, for example) due to the fact that the data is obtained by appropriately differentiating the displacement fields. The VIC system is not expected to have the resolution to capture accurate strain information in the carbon fiber areas of the wing: any non-zero data in these areas is probably due to the spatial smoothing algorithm employed by the VIC system. At 7 m/s,  $\sim 0.5\%$  stretching is measured between each batten toward the leading edge, where the local inflation is largest. Higher values are seen toward the root and the tip. At higher wind tunnel speeds, a large stress concentration develops between the rigid root and the first batten, resulting in 3% stretching. Indeed, potential de-bonding of the membrane skin from the carbon fiber skeleton at this location on the wing had to be closely monitored during testing.

Local angles of attack measured along the semi-wing of wing 1 are given in Figure 3-6 for a variety of wind speeds and global wing angles of attack (measured at the rigid root). At 7 m/s and  $0^\circ$  angle of attack, the majority of the wing has twisted such that the flexible wing sections have a negative angle of incidence. Though there appears to be no appreciable relationship

between twist and span location for this flight condition, a clear trend is seen for the remaining cases in Figure 3-6. The nose-down twist peaks between 40% and 60% of the semi-span, and recovers some of its original (undeformed) incidence at the wing tip. The twist gradients are fairly large at this location, potentially indicating the effect of the tip vortex swirling [15]. For higher speeds (12 m/s), a substantial portion of the wing at 5° and 10° is twisted to a negative incidence. At the higher angle of attack (15°) the twist recovery at the wingtip is less than seen in previous cases. Results for higher angles of attack (which will be discussed in terms of loads measurements) are unavailable with the low-speed VIC system available for the current research: periodic vortex shedding [16] at these angles leads to a substantial wing vibration.

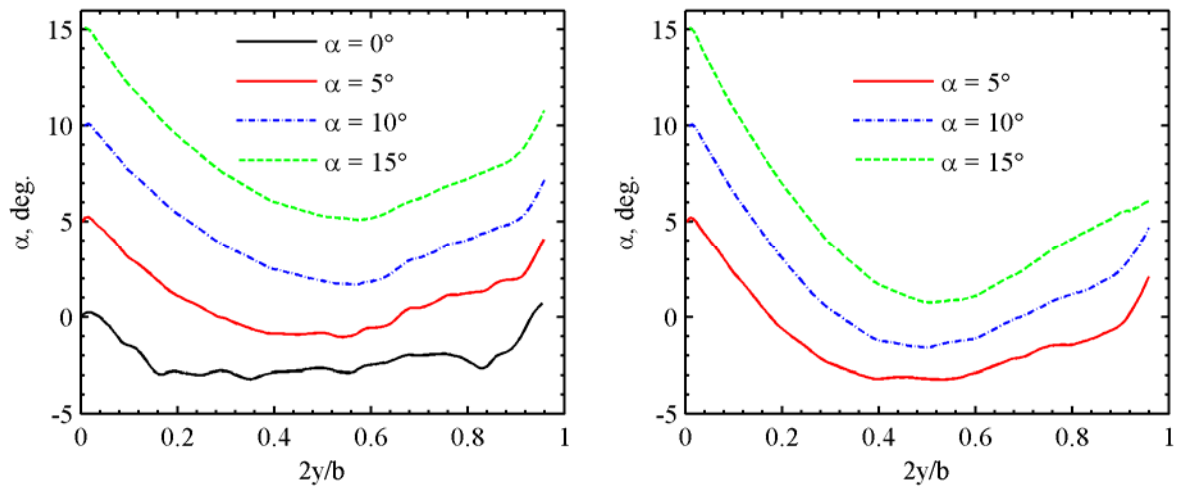


Figure 3-6. Local angle of attack along the semi-wing of wing 1 at 7 m/s (left) and 12 m/s (right).

Similar data is given in Figure 3-7 for the maximum camber at each spanwise station, as defined in Figure 3-3. The camber at  $2y/b = 0$  is that of the rigid wing. As before, trends at  $0^\circ$  are unclear: the wing shows a slight increase in camber (due to inflation) toward the root and the wingtip, but elsewhere slightly de-cambers. For the remainder of the cases considered in Figure 3-7, a clear undulation in the curve distinctly separates areas of membrane and carbon fiber. The adaptive washout noted in Figure 3-6 is not a rigid twisting of each section, but instead is

facilitated by chordwise bending of each batten. This causes the wing to de-camber in a global sense, though local increases in camber are seen due to the inflation of the membrane skin in Figure 3-7. This behavior follows a similar trend to that seen above: the greatest deformation is between 40% and 60% of the semi-span, the wing recovers some of its original shape toward the wingtip, and deformation generally increases with angle of attack and flight speed. Unlike the adaptive washout however, the cambering of the wing (for a given flight speed) is relatively independent of angle of attack up to 30% of the semi-span.

Similar data is given in Figure 3-8, for the spanwise bending of the wing (defined in Figure 3-3). Deformations are fairly large (upwards of 15% of the root chord), and monotonically increase with angle of attack and flight speed (pre-stall). The slope of the curve decreases toward the wing tip, indicative of the fact that that aerodynamic loading becomes very small in this area, as previously noted.

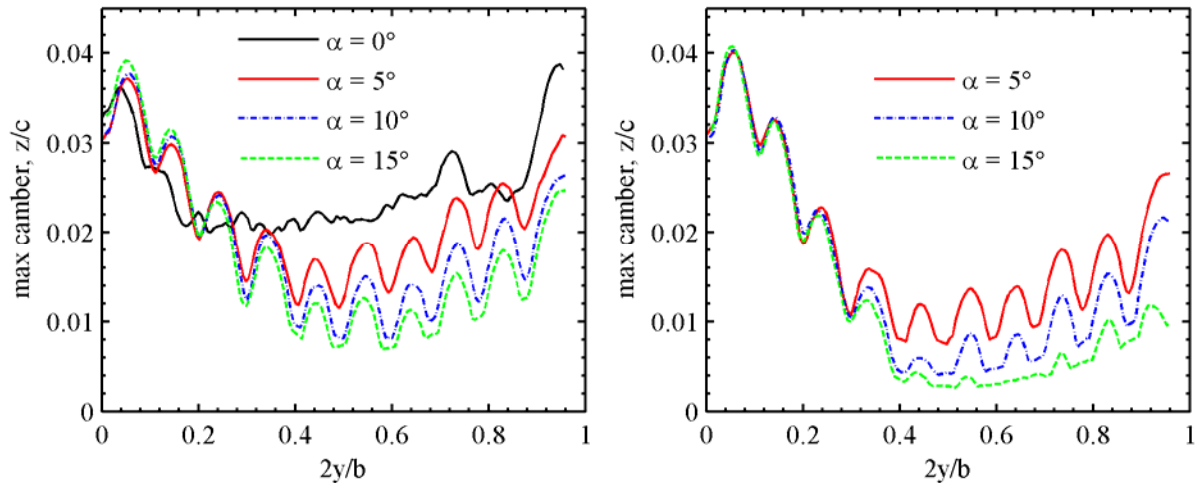


Figure 3-7. Local maximum camber along the semi-wing of wing 1 at 7 m/s (left) and 12 m/s (right).

Lift coefficients for wing 1 and a rigid wing, for the entire sweep of speeds and angles of attack, are given in Figure 3-9. The resolution of the force balance is estimated to be 0.01 N, and error bars (not shown) are estimated to be 5% of the mean reported value. No substantial

dependence upon the Reynolds number is noted for the lift of the rigid wing in the pre-stall regime; the extreme Reynolds numbers are reported in Figure 3-9. The rigid wing at the lower speed stalls slightly earlier ( $12^\circ$ ), and shows a larger drop in lift after stall. This process repeats itself again at  $21^\circ$  (presumably after the boundary layer vortex separates from the wing and convects into the wake), after which the lift of the rigid wing does not change substantially, regardless of Reynolds number.

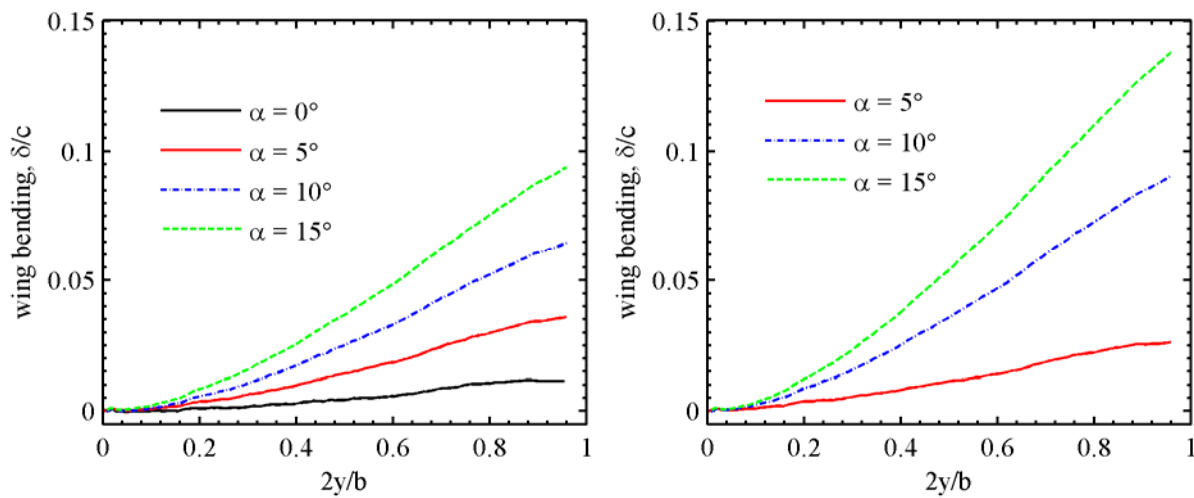


Figure 3-8. Local bending along the semi-wing of wing at 7 m/s (left) and 12 m/s (right).

For the membrane wing, a large variation in the lift curve can be seen with different flight speeds, evinced by the drastic changes in shape seen in Figure 3-6 – Figure 3-8. All of the flexible cases have a shallower lift slope and a larger stalling angle than the rigid wing, though the lowest speed (and hence the smallest deviations in wing shape) approaches the rigid case. The large stalling angles are further verified by the results of Hu et al. [13], who find attached flow over load-alleviating membrane wings at high angles of attack.

In general, both  $C_L$  and  $C_{L\alpha}$  decrease with higher speeds, due to the adaptive washout and the de-cambering of the wing. The latter metric decreases to the very low value of  $1.98 \text{ rad}^{-1}$  for high flight speeds. The angle of attack at zero lift generally increases (from  $-2^\circ$  to  $5^\circ$ ), and

negative lift is seen at positive angles of attack for a number of the cases in Figure 3-9. Even though the un-deformed wing is positively-cambered, a substantial portion of the semi-wing elastically twists to a negative angle of attack, as seen in Figure 3-6. Wing stall is delayed as well, from  $15^\circ$  at 5 m/s to  $32^\circ$  at 13 m/s. Differences in aerodynamic performance between 13 m/s and 15 m/s are minimal (with the exception of stalling angle, as the latter stalls about  $5^\circ$  earlier), which may indicate that the wing has reached an elastic limit.

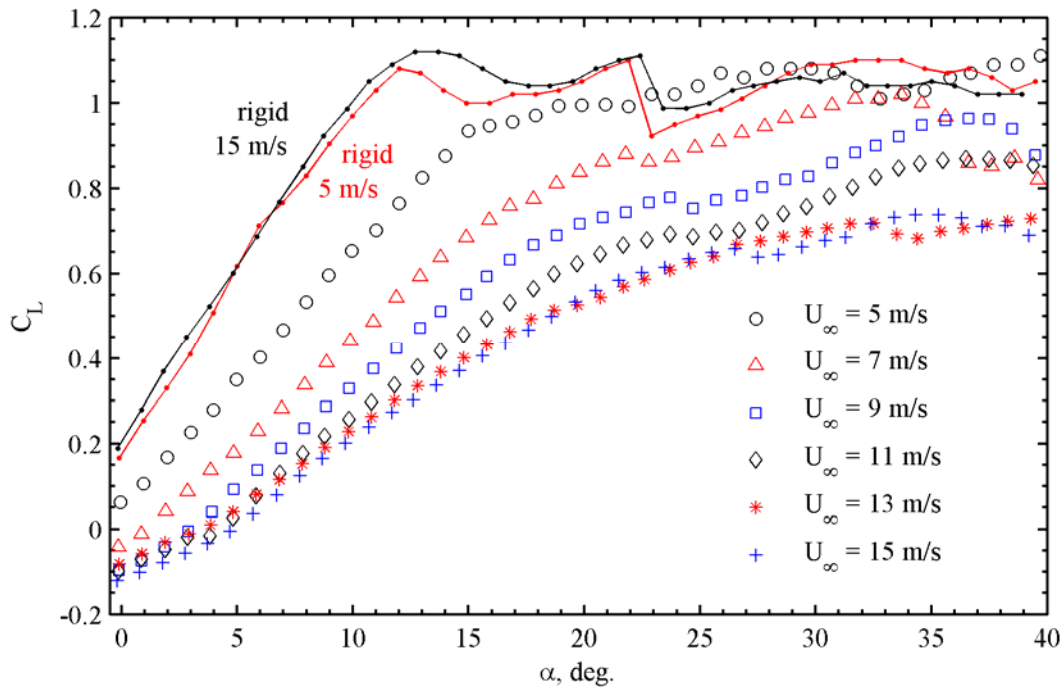


Figure 3-9. Lift coefficients of wing 1: angle of attack is measured at the rigid root.

### 3.1.2 Effect of Batten Stiffness

Having ascertained in the previous section how a single membrane structure (wing 1) behaves under a variety of flight conditions, attention is now turned to differing wing structures. Specifically, a comparison of wings 1, 2, 3 and 4 (as seen in Figure 3-2), which alter the stiffness of the wing uniformly along the span by increasing the number of plies used to construct each carbon fiber batten. VIC results are given in Figure 3-10, in terms of the chord-normalized

deformed wing shape ( $z/c$ ) at  $10^\circ$  angle of attack, and 7 and 12 m/s flight speed. It should be noted that the plots show the deformed wing shape, rather than the displacement contours of Figure 3-4. Corresponding wing twist, cambering, and bending data is given in Figure 3-11, Figure 3-12, and Figure 3-13, respectively.

The most striking feature of the comparison between wings 1-4 is the extremely large wing bending of the stiffer structures. Under the same flow conditions, wing 1 bends to 8% at the tip, while wing 4 bends to 72%. This is due to the load-alleviating properties of the thinner battens, which adaptively washout along the trailing edge to decrease the sectional lift. The thicker battens do not washout as much, and so the wing responds to the load by bending along the span. This is emphasized by the contour lines of Figure 3-10, which progressively shift from being parallel to the trailing edge (washout) to perpendicular (spanwise bending), as the number of layers in each batten is increased from 1 to 4.

Furthermore, as seen in Figure 3-11, wings 2 and 3 show some degree of adaptive wash-in at 7 m/s (particularly wing 3), though this motion is gone at the high dynamic pressure. It is not clear from Figure 3-10 if the positive twist of each wing section (which is just measured by comparing the leading and trailing coordinates) is due to a specific wash-in of the battens, or a more global wing shaping behavior. This latter phenomenon may arise from a bend-twist coupling behavior, perhaps due to the nonhomogenous wing structure. Though the leading edge “T” is constructed of orthotropic carbon fiber, all of the layers of the plain weave laminate are oriented in a  $\pm 45^\circ$  orientation, which will not contribute to the bend-twist coupling [3]. On a second note, in Figure 3-11 for the 12 m/s case, the contour lines are angled, which is once again caused by the bend-twist coupling. However, this angle is not observed in the other wings.

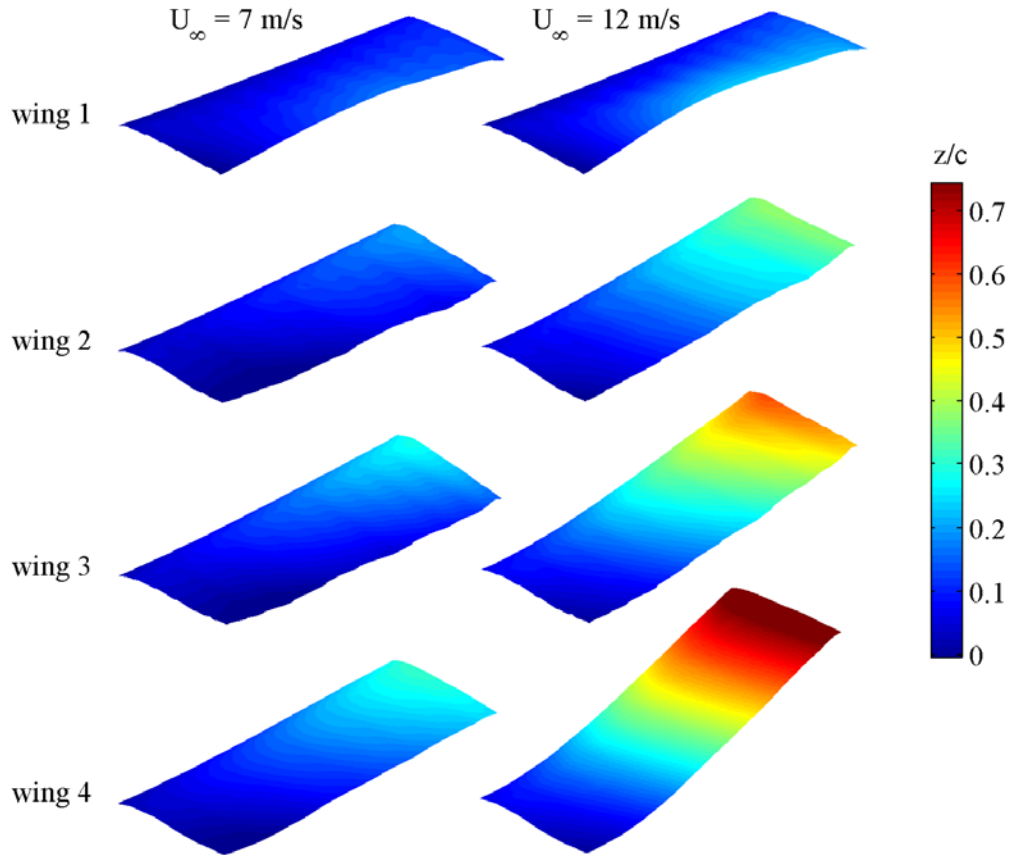


Figure 3-10. Chord -normalized deformed semi-wing shape ( $z/c$ ),  $\alpha = 10^\circ$ .

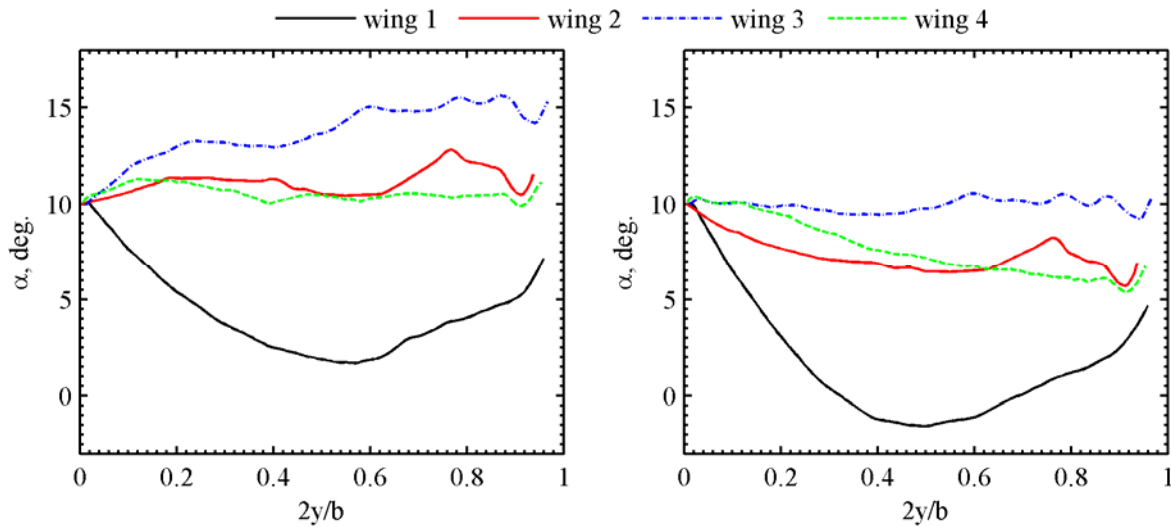


Figure 3-11. Local angle of attack along the semi-wing at 7 m/s (left) and 12 m/s (right),  $\alpha = 10^\circ$ .

Additional aeroelastic load augmenting is evident in Figure 3-12, where wings 2-4 show positive adaptive cambering, as opposed to the general de-cambering deformation seen by wing

1. At 12 m/s, the amplitude of the local undulations is much larger as well (though the pattern is unobservable in Figure 3-10, as the displacements are dwarfed by the global spanwise bending). This is to be expected, as the stiffer battens provide a more rigid boundary condition for the local membrane inflation. Though not explicitly discussed in this section, the spanwise strains that develop within the membrane skin (as seen in Figure 3-5, for example) grow with the spanwise bending, as expected. Wing 4 at 12 m/s sees 12% stretching at the trailing edge of the root, a figure which is well above the validity of a linear stress-strain relationship; a hyperelastic constitutive equation governs the response [3].

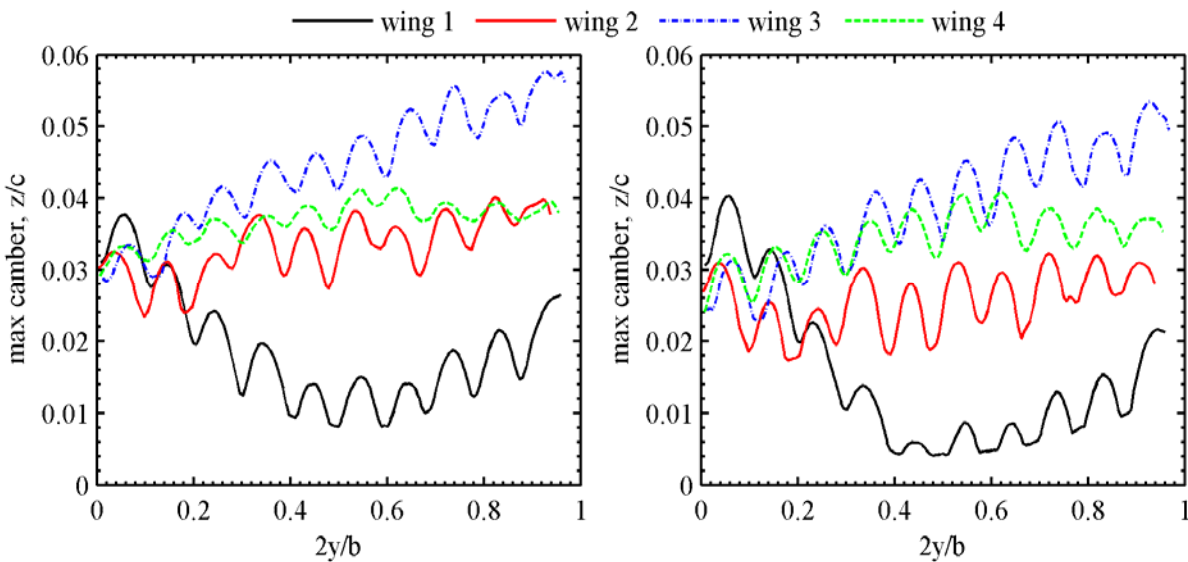


Figure 3-12. Local maximum camber along the semi-wing at 7 m/s (left) and 12 m/s (right),  $\alpha=10^\circ$ .

The measured lift coefficients for the four membrane wings, as well as the rigid wing, are given in Figure 3-14, for wind speeds of 5, 9, and 13 m/s. At the lowest Reynolds number ( $3.3 \cdot 10^4$ ), wings 2, 3, and 4 all have a higher pre-stall lift than the rigid wing, as evidenced by the load augmenting passive shape deformation trends seen above: trailing edge wash-in (Figure 3-11) and positive cambering (Figure 3-12). As wing 4 shows a smaller amount of wash-in than

wings 2 and 3, the increase in lift is also smaller. Only wing 1 is able to appreciably delay stall, and all 5 structures show similar post-stall behavior.

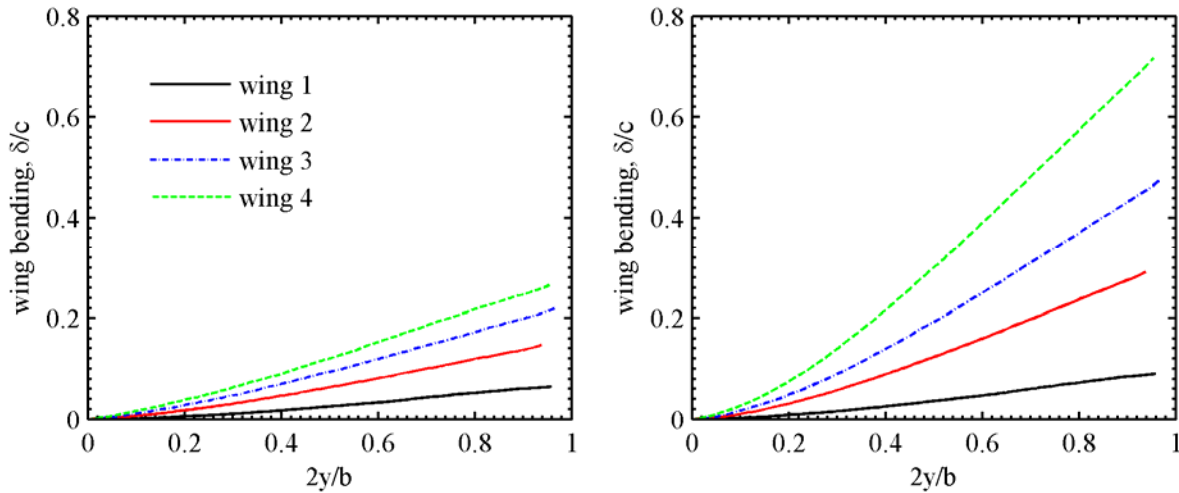


Figure 3-13. Local bending along the semi-wing at 7 m/s (left) and 12 m/s (right),  $\alpha = 10^\circ$ .

At the median Reynolds number (corresponding to 9 m/s), the results are strikingly different. Wing 3 stalls at roughly the same location seen at the lower speed, but past this angle of attack the lift continues to monotonically grow through the largest tested angle of 40°, reaching an impressive coefficient of 2.2. Wing 4 shows similar behavior, but has a drastic drop in lift at 37°. Similar post-stall behaviors for membrane micro air vehicle wings are noted in the work of Waszak et al. [22] The reasons for these striking results are as of yet unclear. The passive deformation may provide smooth attached flow at large angles of attack, as noted in the PIV work of Hu et al. [13] Alternatively, static and/or dynamic mechanisms (i.e., wing vibration) may be at work to keep a leading edge vortex attached to the wing, as seen in classic dynamic stall studies [23]. The abrupt drop in lift of wing 4 at high angles would indicate the latter, potentially caused by a sudden detached vortex. As substantial as these results are, the beneficial post-stall performance is very mutable and fragile. At the highest Reynolds number seen in Figure 3-14, the phenomenon is gone: the stalled region is very flat, as before.

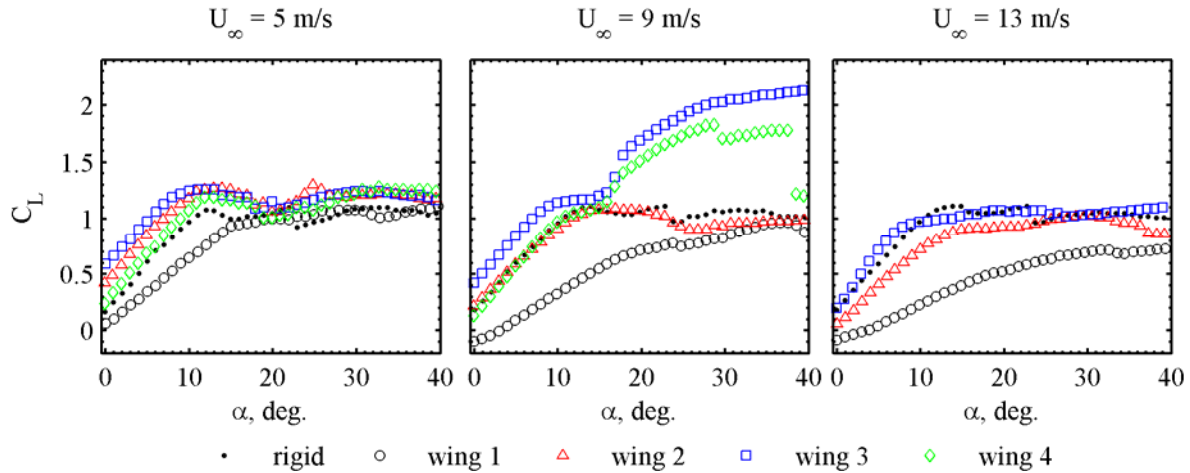


Figure 3-14. Lift coefficients: angle of attack is measured at the rigid root.

### 3.1.3 Spanwise Stiffness Gradient

This section studies a comparison of wings 5, 6, and 7; each provides a spanwise gradient of batten stiffness. As above, wing twist, cambering, and bending are given in Figure 3-15, Figure 3-16, and Figure 3-17, respectively, along with data from wing 1 for comparisons. In terms of spanwise twist and cambering distributions, wings 5 and 6 are mirror images of each other. The battens of wing 5 are very stiff toward the root, resulting in adaptive wash-in and positive cambering (data for this wing is not available at the higher dynamic pressure, due to excessive vibrations). Toward the wing tip, the battens are very thin, leading to washout and de-cambering. Opposite trends are seen for wing 6, whose stiffness is clustered at the tip. Differences in wing bending (Figure 3-17) between wings 5 and 6 are marginal, with the former showing a slightly larger tip deflection.

The structures of wings 1 and 7, as reviewed above, are identical with the exception of the wingtip batten: a single layer of carbon fiber is used for wing 1, while four are used for wing 7. As expected then, twist and camber trends show little difference up to 50% of the semispan. At the wing tip, the shape of wing 7 generally recovers to the undeformed shape: the local incidence returns to  $10^\circ$ , and the camber returns to 3%: the wing is too stiff to either alleviate or augment

the flight loads. The bending curves of wings 1 and 7 (Figure 3-17) are coincident, due to the fact that adaptive pressure redistributions from wing 1 to wing 7 primarily occur at the wing tip, where the forces may be too small to make much of a difference.

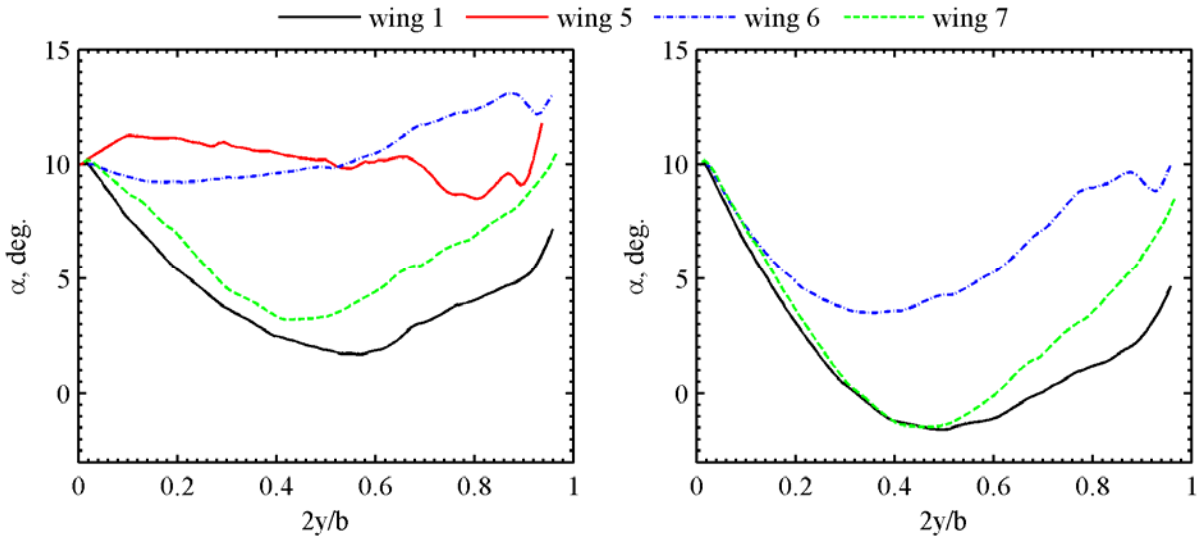


Figure 3-15. Local angle of attack along the semi-wing at 7 m/s (left) and 12 m/s (right),  $\alpha = 10^\circ$ .

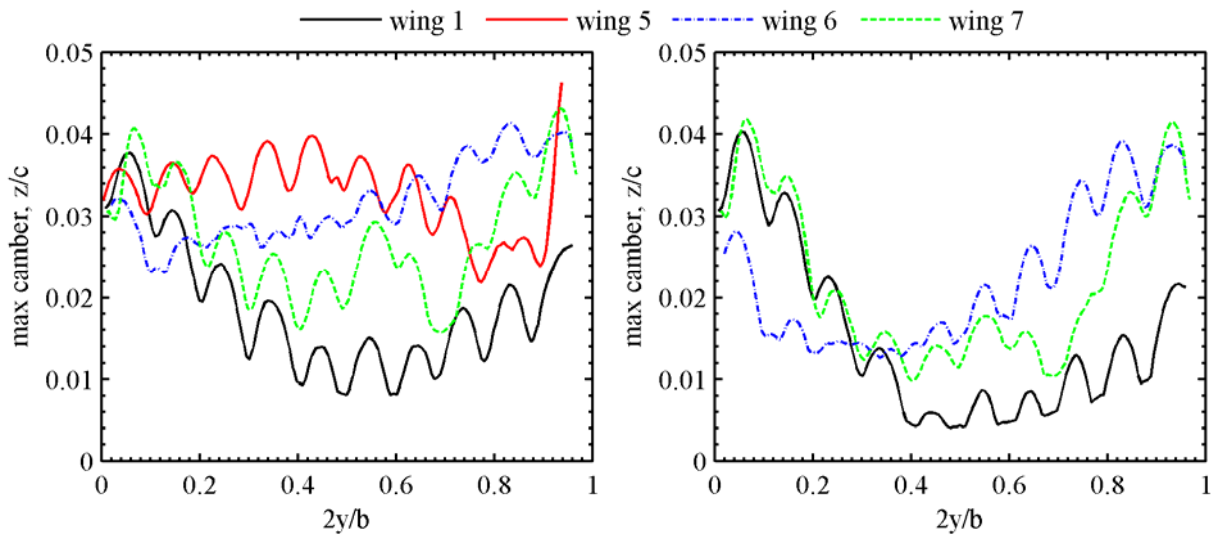


Figure 3-16. Local maximum camber along the semi-wing at 7 m/s (left) and 12 m/s (right),  $\alpha = 10^\circ$ .

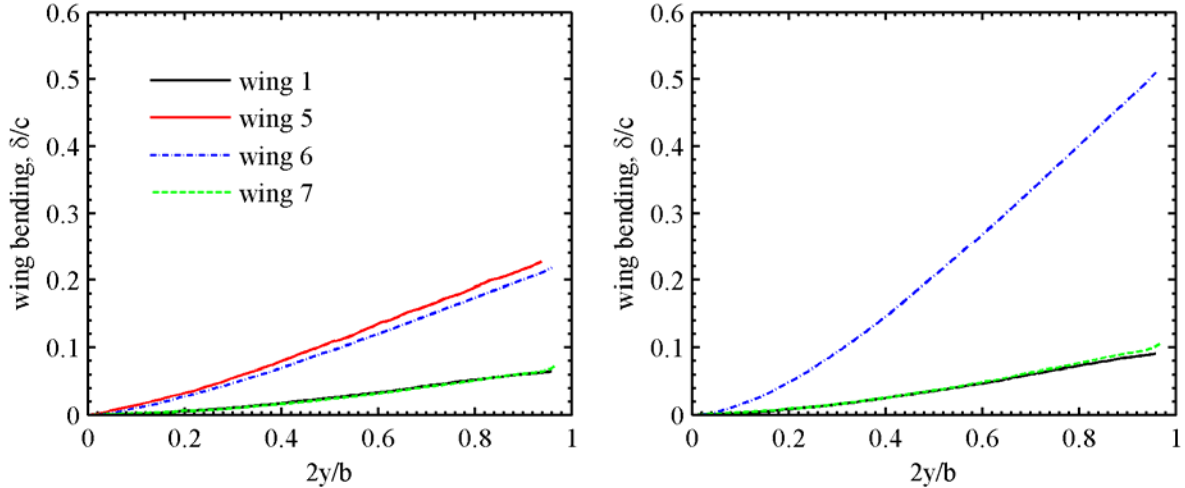


Figure 3-17. Local bending along the semi-wing at 7 m/s (left) and 12 m/s (right),  $\alpha = 10^\circ$ .

Coefficient of lift data for the three wings, as well as the rigid wing and wing 1 for comparisons, are given in Figure 3-18, for three flight speeds of 5, 9, and 13 m/s. Wings 1 and 7 show substantial differences, a surprising fact given that the majority of the wing structure is identical. Pre-stall, the lift curves are very similar, but wing 7 stalls at a significantly higher lift coefficient (at 9 m/s), and at 13 m/s, the wing never appears to stall. This result would almost certainly indicate the strong role of tip vortex swirling in the aeroelastic behavior of the membrane wing. Wing 6, which shares a similar (however more gradual) stiffness gradient to wing 7, shows a comparable trend, though muted. Particularly at 9 m/s, the maximum attainable lift is very large, but occurs (stalls)  $10^\circ$  before wing 7. For the opposite stiffness gradient provided by wing 5, the lift behavior is similar to wings 1 and 7 for very small angles of attack (at 9 and 13 m/s), but then shows an extremely steep lift slope and moderately non-linear behavior (pre-stall). Compared to the rigid wing, wing 5 stalls very early, and has a relatively low maximum lift coefficient. The reasons for this behavior are unclear, nevertheless as noted by Ormiston [24], the steep lift slopes may make controllability of the membrane wing very difficult.

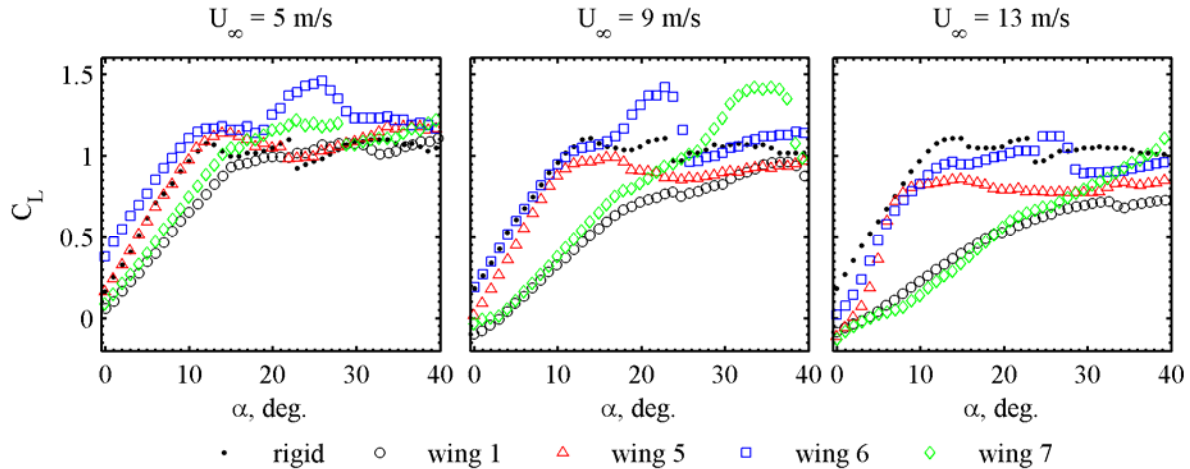


Figure 3-18. Lift coefficients: angle of attack is measured at the rigid root.

### 3.1.4 Batten Spacing and Trailing Edge Shape

This section studies the effect of removing battens from the wing structure; specifically a comparison of the lift-producing abilities of wings 2, 8, and 9 (as seen in Figure 3-2). All three wings have two-layer battens, but the latter two only have five evenly-spaced strips of carbon fiber, rather than ten. An excessive amount of un-constrained membrane skin will, as the dynamic pressure increases, lead to a large-amplitude vibration along the trailing edge, similar to the flapping motion of a flag. Such motions preclude the use of the VIC system used in this work. Potential reasons for this complex phenomenon are discussed by Fitt and Pope [18]; experimental observations are given by Mastramico and Hubner [15], who suggest the use of a scalloped trailing edge (commonly seen in a bat's membrane wing [10]) to remove the portion of the wing that is prone to excessive vibration. As discussed above, scalloping is present in wing 9. A general lift coefficient comparison is seen in Figure 3-19.

Scalloping generally provides a larger pre-stall lift coefficient than wing 8 for all flight speeds; at the lowest speed considered (below the critical dynamic pressure that leads to vibration), the wing has higher lift than wing 2 as well. Mastramico and Hubner [15] indicate that a scalloped wing has consistently lower drag than other tested wing structures (potentially

due to a favorable tuning between the shear layer and the membrane skin), suggesting a high aerodynamic efficiency. The un-scalloped wing 8 typically has the shallowest pre-stall lift slopes of the wings compared in Figure 3-19, but the largest maximum post-stall coefficients as well. This latter point may be a beneficial result of the wing vibration, which has been shown by Munday and Jacob [25] to decrease the size of separation bubbles at low Reynolds numbers for certain reduced frequencies.

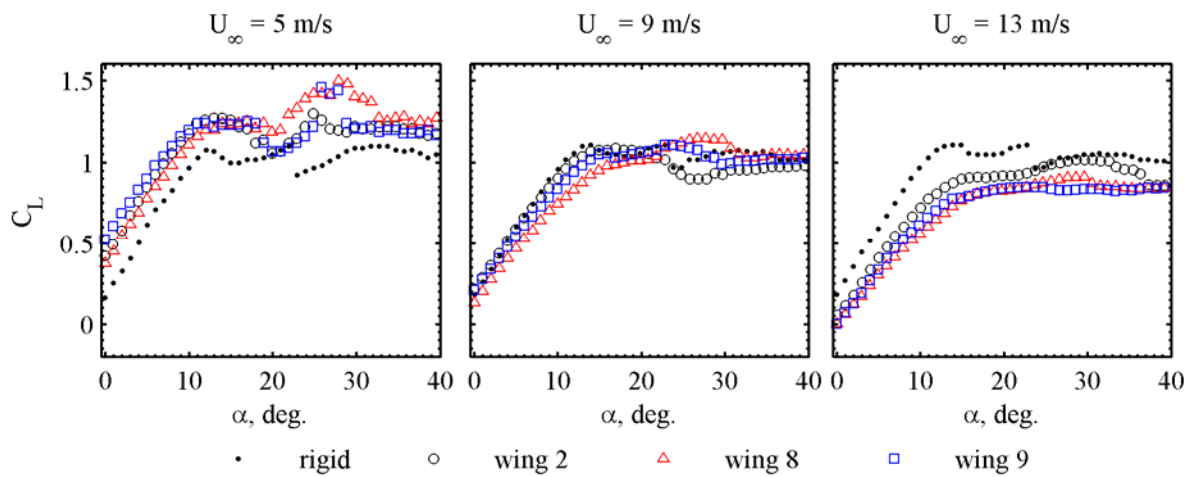


Figure 3-19. Lift coefficients: angle of attack is measured at the rigid root.

### 3.2 Silicone Perimeter Reinforced Membrane Wing Results

This research documents the correspondence between the crinkle angle, lift, drag, lift over drag ratio, pitching moment, and pitching moment slope. Though so many different combinations are possible, such as using altered specimens with varying thicknesses of silicone, any kind of desired materials, or various geometrical shapes (ellipses, rectangles, or random patterns), three different specimens are taken under consideration for this research: crinkled silicone membrane, another crinkled membrane with a rigid carbon-fiber plate beneath, and isotropic thin silicone elliptical membrane (Figure 3-20). For lower speeds (5 m/s – 13 m/s),

results were very similar to rigid wing's since the material deformations were not significant; therefore, the tests were conducted solely at a higher speed of 15 m/s.

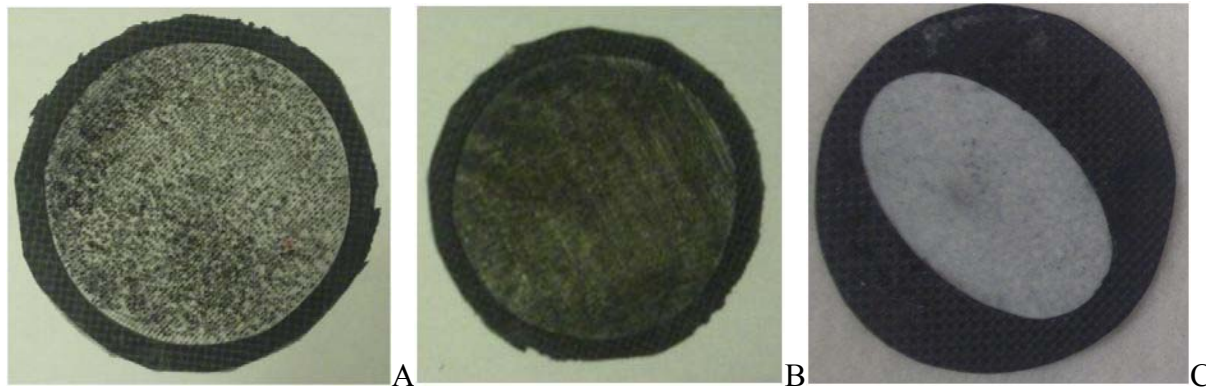


Figure 3-20. Specimens sandwiched in the wing apparatus. A) crinkled silicone membrane glued on a carbon-fiber ring, B) crinkled silicone membrane glued on a two layer circular carbon fiber plate, C) isotropic silicone membrane glued on a two layer carbon-fiber plate that has an elliptical hole.

The notation used for the wing structures are shown in Figure 3-21 and Figure 3-22. The crinkle angle is measured with respect to the x-axis of the wing along the chord line. As an example, in Figure 3-21, 45° crinkle angle is drawn while for the elliptical wing apparatus, the angle between the minor axis and x axis is measured; therefore, in Figure 3-22 the angle,  $\gamma$ , is equal to 135°. The reason for this notation is because under hydrostatic pressure at a crinkle angle of 135°, an exaggerated elliptical shape in Figure 3-22 is expected although loads experienced by the wing are not hydrostatic in the wind tunnel.

As shown in Figure 3-20, specimen A was used on the wing apparatus to explore the aerodynamic loads and deformation at different crinkle angles, specimen B was installed to see the surface effects, and finally specimen C was placed in the wing apparatus to examine if the elliptical angle has an effect on the wing performance. Afterward all the results were discussed in detail showing images from visual image correlation system (VIC) measurements and wind tunnel experiments.

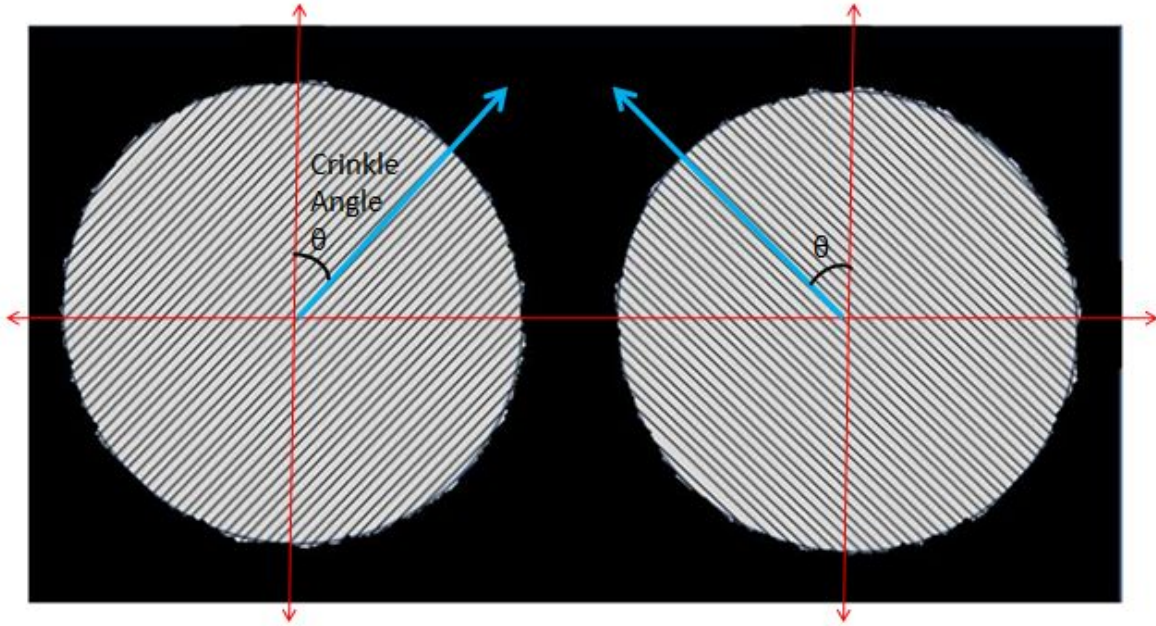


Figure 3-21. Crinkle angle notation for both the silicone membrane wing and the silicone membrane with a rigid carbon-fiber plate beneath.

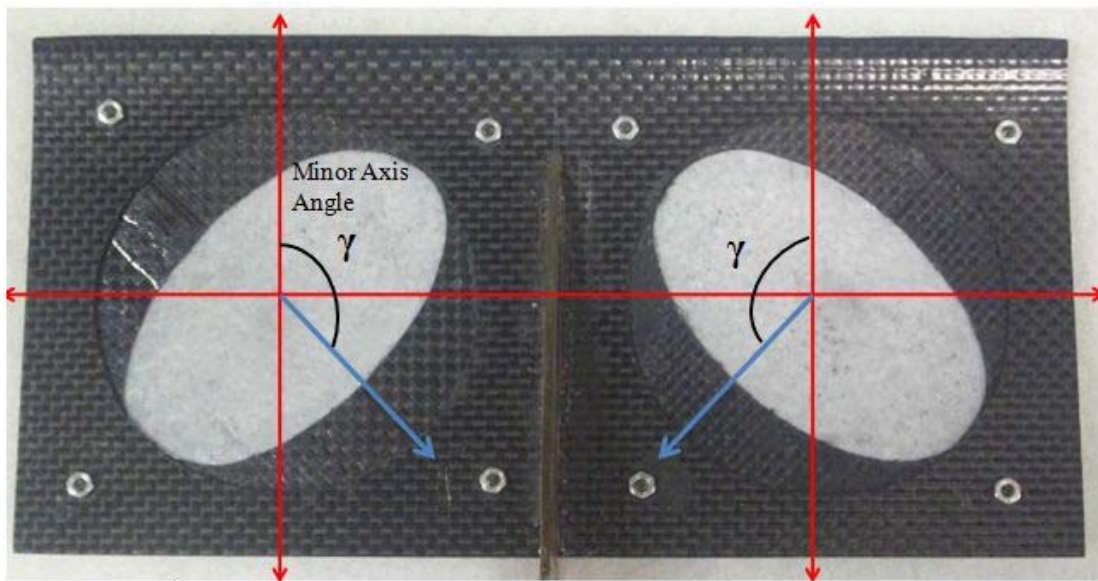
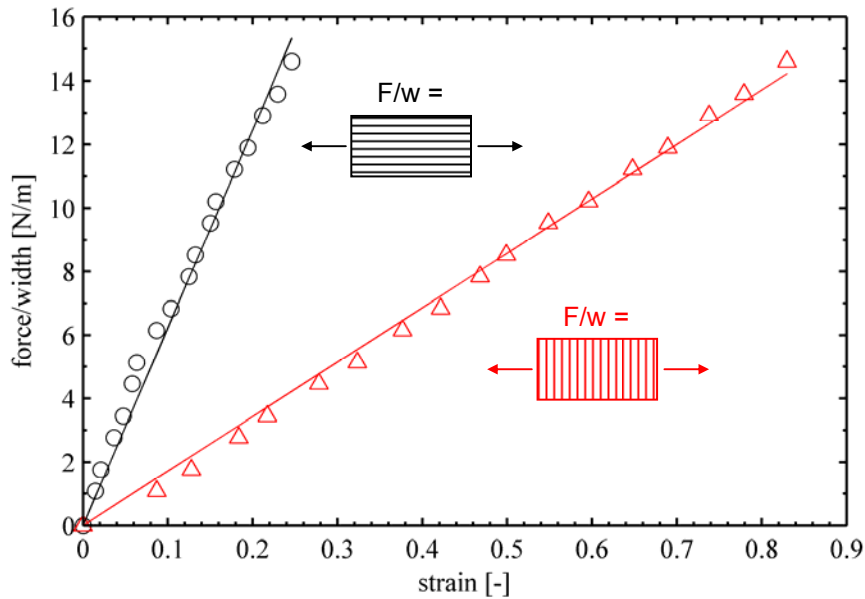


Figure 3-22. Elliptical silicone membrane wing and notation for showing the angle of the ellipse.

### 3.2.1 Crinkled Silicone Membrane Specimen

Before the wind tunnel and visual image correlation experimentations, the properties of the fabricated anisotropic material were studied by Stanford et al. [26] Two specimens of

membrane were cut to be subjected to a tension test under different loads in two directions, one direction being in the line of crinkles and the other perpendicular to the crinkles. The elongations were measured, recorded, and analyzed. The result was crinkles aligned with the load provided 3.6 times higher stiffness (Figure 3-23).



*Image Courtesy by Stanford, Bret and Ifju, Peter*

Figure 3-23. Uniaxial stretch test with the crinkle pattern normal to, and parallel to, the loading [26]

### 3.2.1.1 Visual image correlation (VIC) testing

This experiment was first tried with no carbon-fiber ring around the specimen; however, only a slight tension difference caused a large discrepancy on the drag data. Therefore, to keep the tension exactly as the same as the previous trial of crinkle angle, a ring was glued around the membrane. Afterward, the wing apparatus was ready to be tested under visual correlation system (VIC) for crinkle angles of 0°, 45°, 90°, and 135° at angles of attack of 10° and 15°. For every crinkle angle, a higher angle of attack caused a slightly larger deformation along with a more defined and eccentric elliptical bulge. The larger deformation is caused by larger loads at 15°, and the more eccentric ellipse is caused by the anisotropic material properties though this

geometrical shape was not necessarily expected before the experimentation since the loads are higher toward the leading edge and lower at the trailing edge; therefore, reducing the effects of hydrostatic pressure (Figure 3-24 – Figure 3-31).

The most eccentric elliptical geometry is experienced at the crinkle angle of 90° because the higher loading toward the leading edge is aligned normal to the crinkles, which causes the material to stretch even more in the direction of the chord line (Figure 3-29). On a second note, the epicenter of all the elliptical deformations is closer toward the leading edge, which is a clear indication that the loads are higher toward the front. On the other hand at the crinkle angle of 0° when the crinkles are directly aligned with the higher loading that is toward the leading edge, the bulging is nearly spherical because the tension along the stiffer direction may be similar to the tension in the weaker direction (Figure 3-24 and Figure 3-25). Also, the highest deformation among this set of trials is experienced when the crinkle angle is set to 0° (Table 3-1). The maximum deformation values are also very similar for crinkle angles of 45° and 135° though these two configurations behave differently in terms of aerodynamic performance, which will be discussed in the next section.

Table 3-1. The relationship between angle of attack ( $\alpha$ ), crinkle angle ( $\theta$ ), and the highest deformation value experienced by the membrane ( $w$ ).

AOA, Crinkle Angle	Highest Deformation (mm)
$\alpha=10^\circ, \theta=0^\circ$	13.50
$\alpha=15^\circ, \theta=0^\circ$	15.40
$\alpha=10^\circ, \theta=45^\circ$	12.75
$\alpha=15^\circ, \theta=45^\circ$	13.40
$\alpha=10^\circ, \theta=90^\circ$	12.70
$\alpha=15^\circ, \theta=90^\circ$	13.05
$\alpha=10^\circ, \theta=135^\circ$	12.80
$\alpha=15^\circ, \theta=135^\circ$	13.50

Another trial of VIC testing was done at the crinkle angle of 105° since this configuration provided an interesting result in the lift over drag data (Appendix).

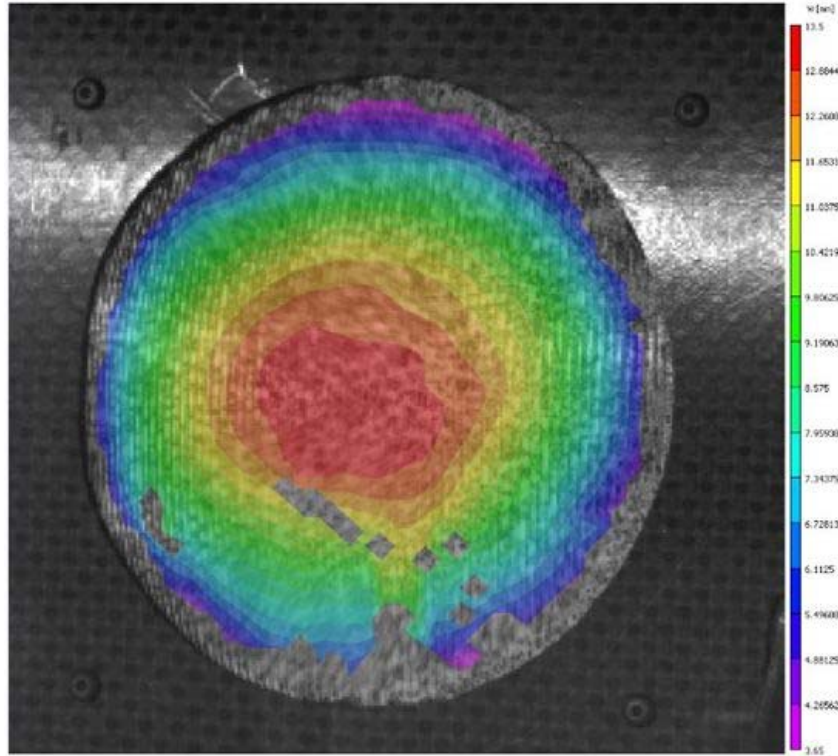


Figure 3-24. Deformation on the left side of the wing at  $\theta=0^\circ$  and  $\alpha=10^\circ$ .

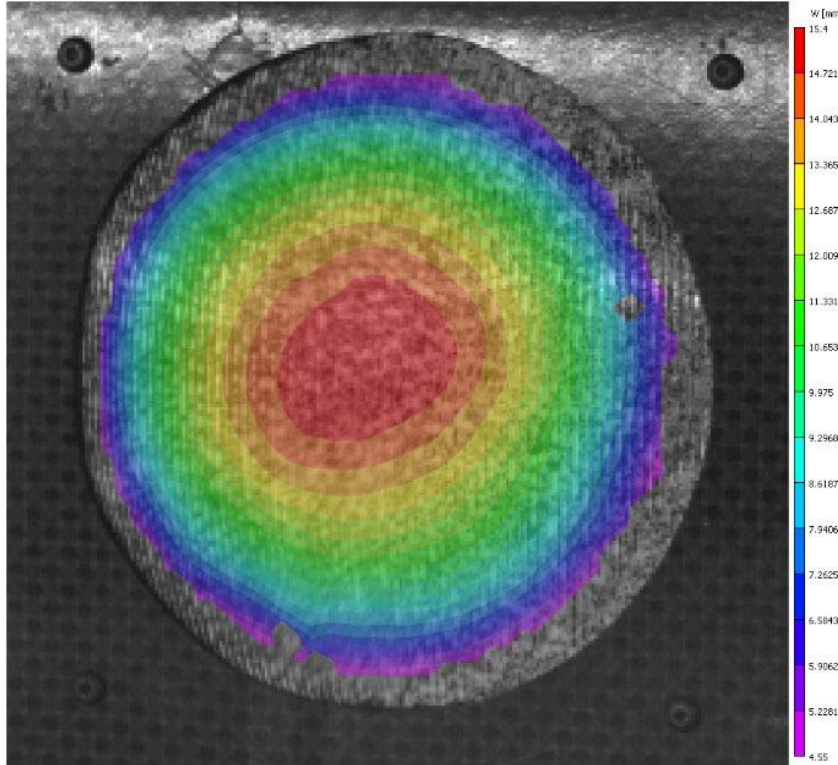


Figure 3-25. Deformation on the left side of the wing at  $\theta=0^\circ$  and  $\alpha=15^\circ$ .

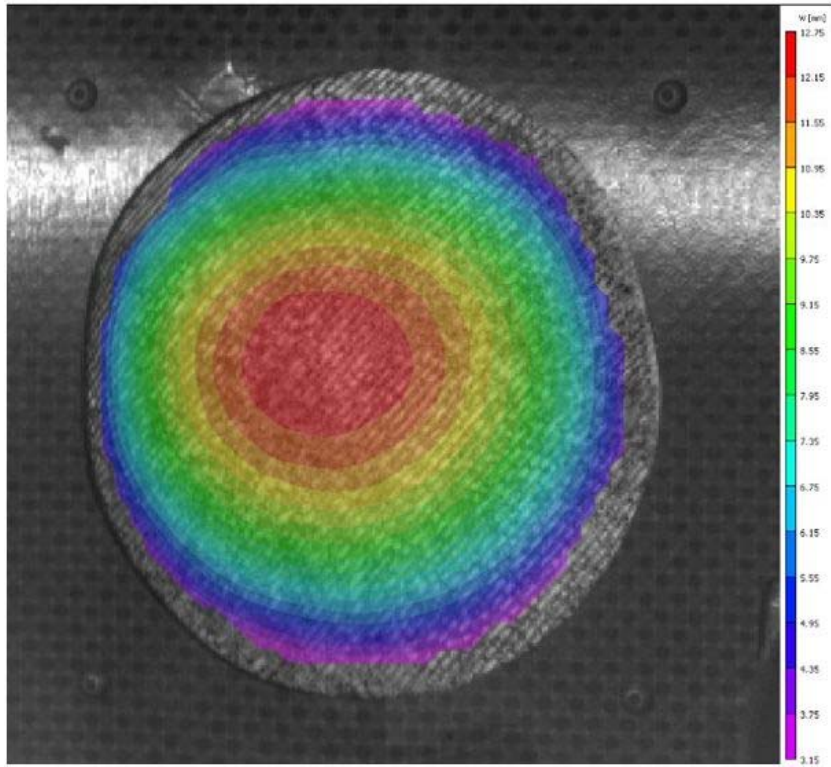


Figure 3-26. Deformation on the left side of the wing at  $\theta=45^\circ$  and  $\alpha=10^\circ$ .

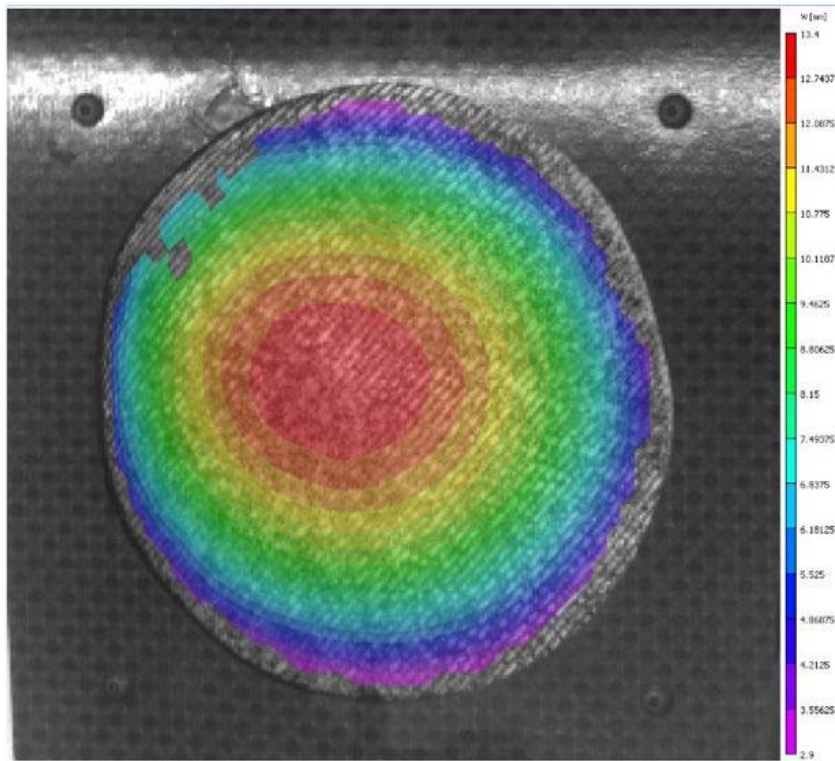


Figure 3-27. Deformation on the left side of the wing at  $\theta=45^\circ$  and  $\alpha=15^\circ$ .

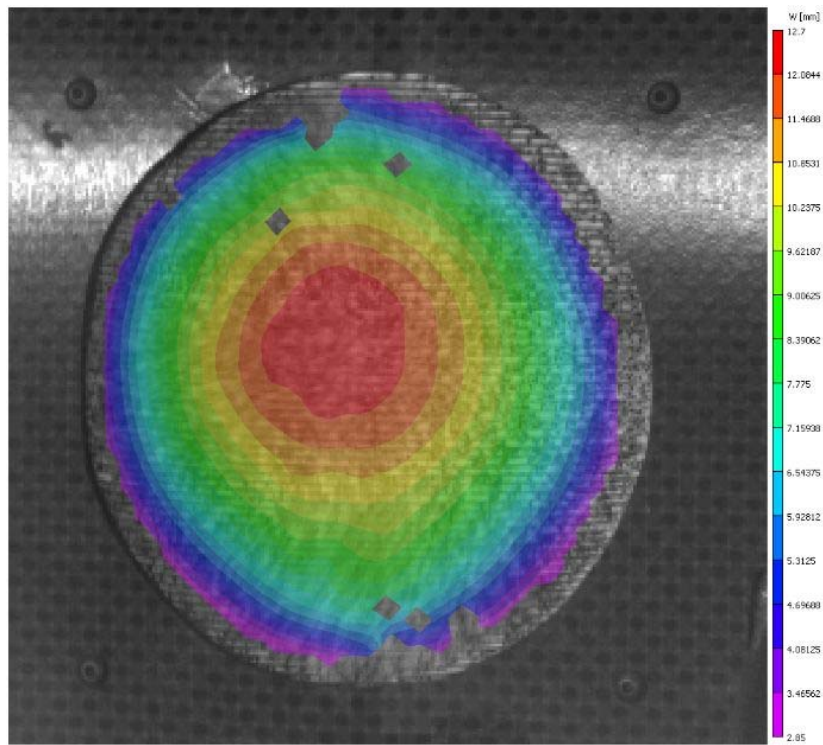


Figure 3-28. Deformation on the left side of the wing at  $\theta=90^\circ$  and  $\alpha=10^\circ$ .

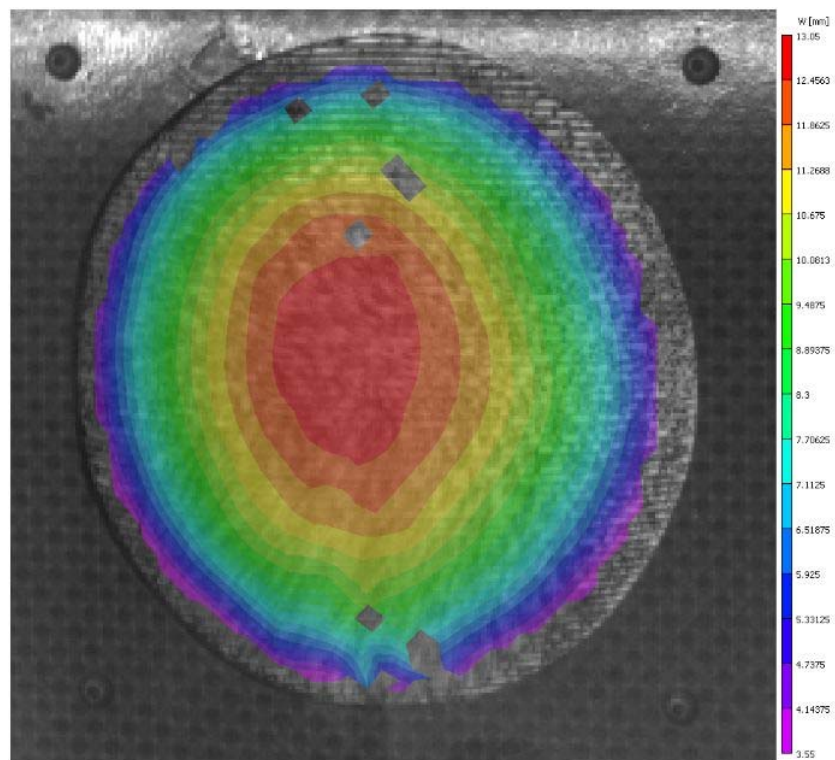


Figure 3-29. Deformation on the left side of the wing at  $\theta=90^\circ$  and  $\alpha=15^\circ$ .

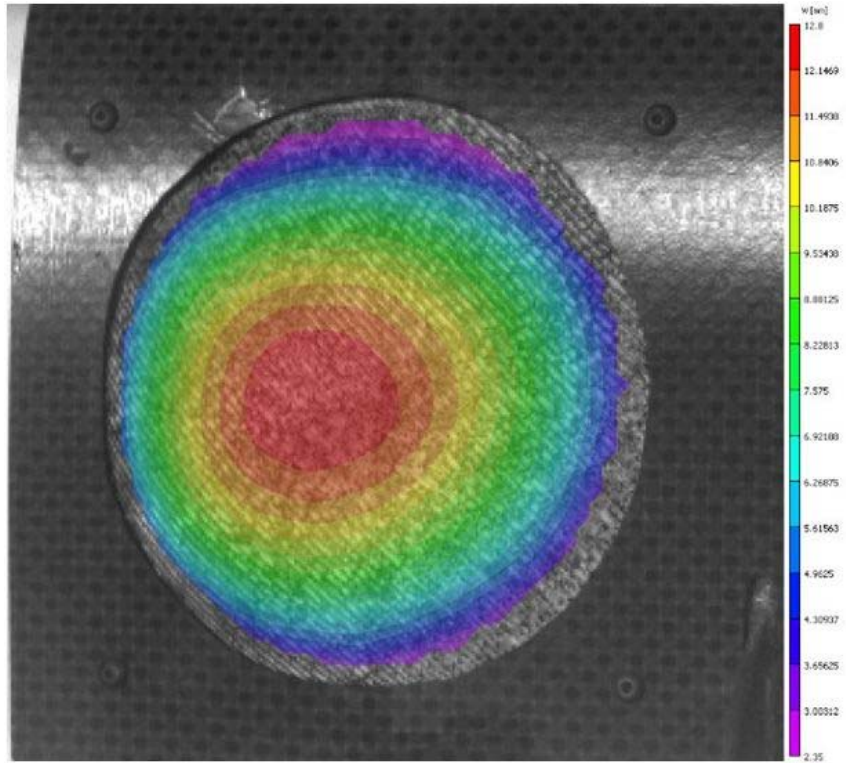


Figure 3-30. Deformation on the left side of the wing at  $\theta=135^\circ$  and  $\alpha=10^\circ$ .

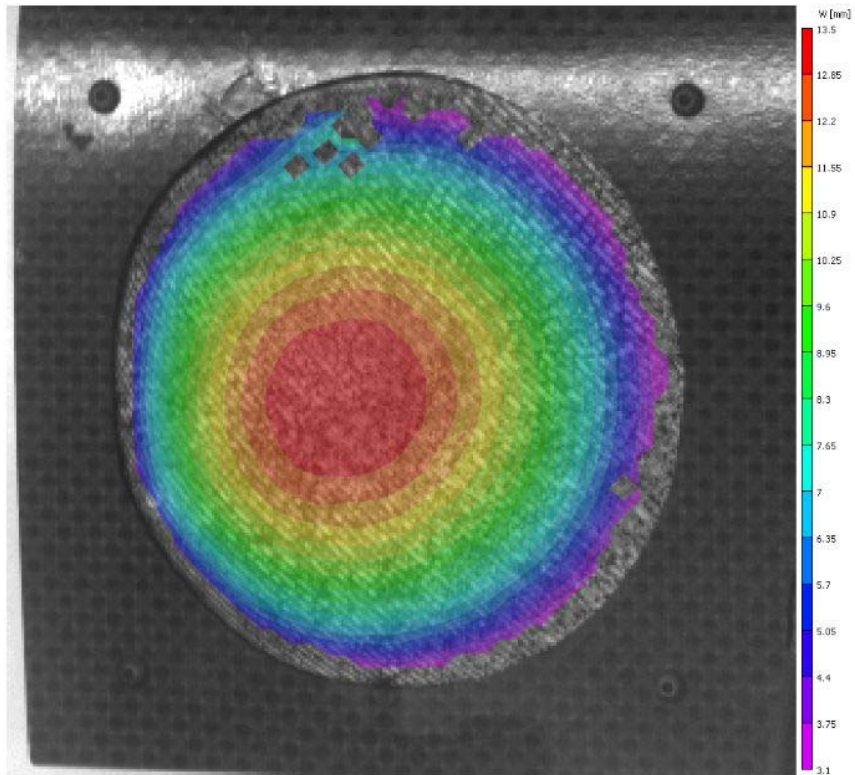


Figure 3-31. Deformation on the left side of the wing at  $\theta=135^\circ$  and  $\alpha=15^\circ$ .

### 3.2.1.2 Aerodynamic load testing

The crinkle angle,  $\theta$ , on the wing apparatus was changed every  $15^\circ$  at 15 m/s for all tests and the data was recorded to be analyzed at an angle of attack array of  $0^\circ$ - $30^\circ$  with increments of 2. In comparison to rigid wing, every crinkle angle of the silicone membrane provided a much higher lift curve because the inflation on the wing caused an increase in camber, thereby increasing the lift coefficients. However, at different crinkle angles the lift history variation is negligible as seen in Figure 3-32. The data for only four different specimen angles are shown since plotting all crinkle angles in the same graph would cause the curves to coincide, thereby creating a chaotic image, which expresses the closeness of all the lift coefficient values. Only when the specimen is set to  $90^\circ$ , slightly aggressive lift curve is observed in the beginning; however, this effect is muted as the stall angle is approached.

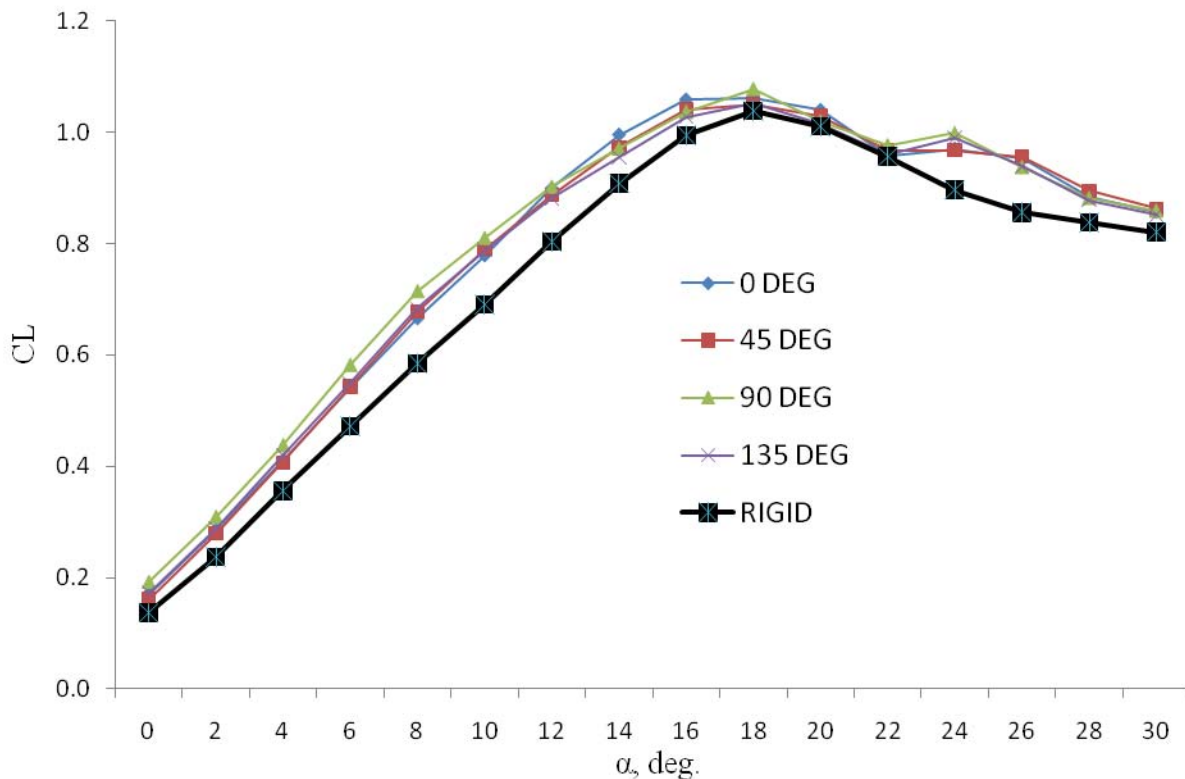


Figure 3-32. Lift curves of four different crinkle angles and rigid wing at 15 m/s.

Though lift curves were very similar, drag data varied substantially between the different angles of the crinkled specimen (Figure 3-33). More flexibility gives higher lift and better static stability since steeper pitching moment curves are observed in Figure 3-34, but more drag and much worse lift over drag coefficients; therefore, there is a trade-off (Figure 3-35). Among the different angles of the specimen when the angle is set to 105°, lift over drag gives the best performance while 90° gives the worst although numerical values of deformation were similar for both cases; however, the shape was closer to a spherical shape when the crinkle angle was set to 105° (Appendix). So, it was suspected that geometrical effects might have been playing a critical role on drag.

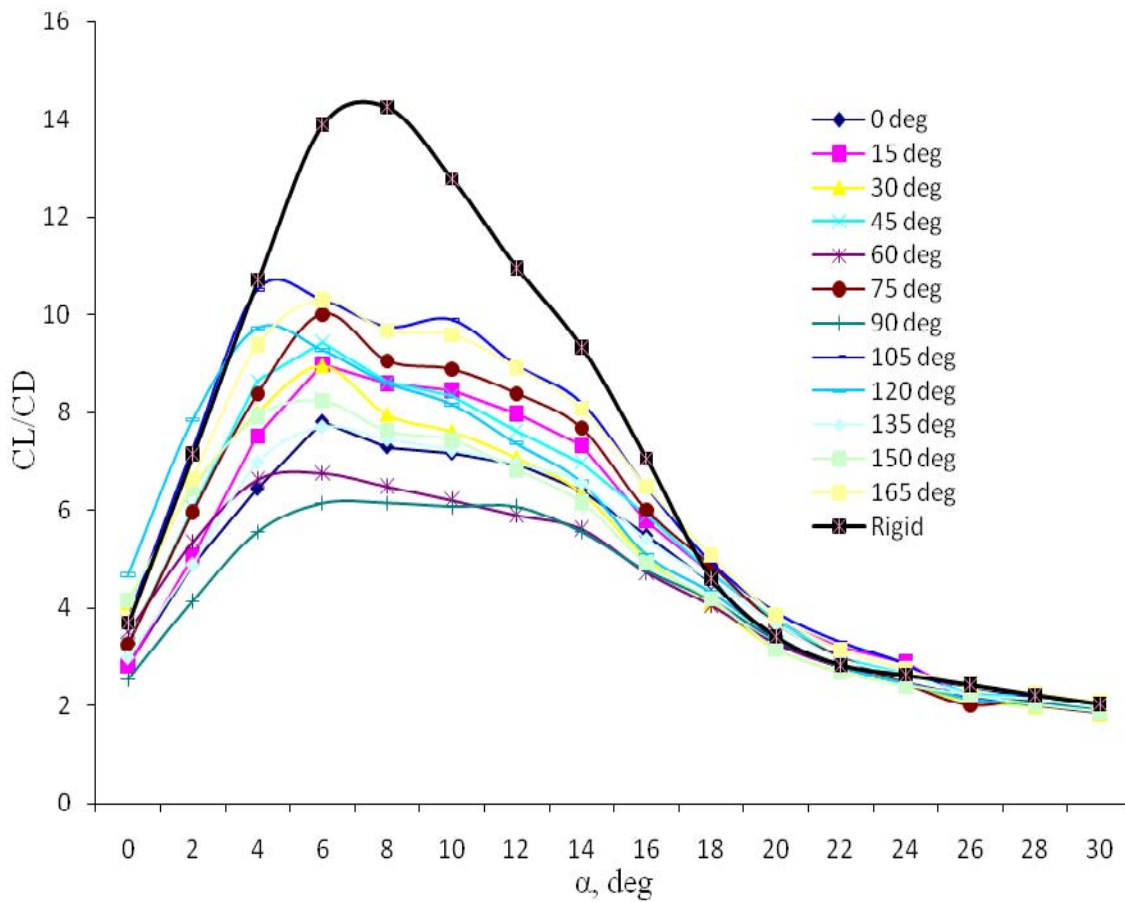


Figure 3-33. Lift over drag curves of all tested angles of specimen and rigid wing at 15 m/s.

The stall angle for every trial changed very slightly in such a way that one may assume stall angle remains the same for all configurations, which corresponds to  $17.5^\circ$  (Figure 3-32).

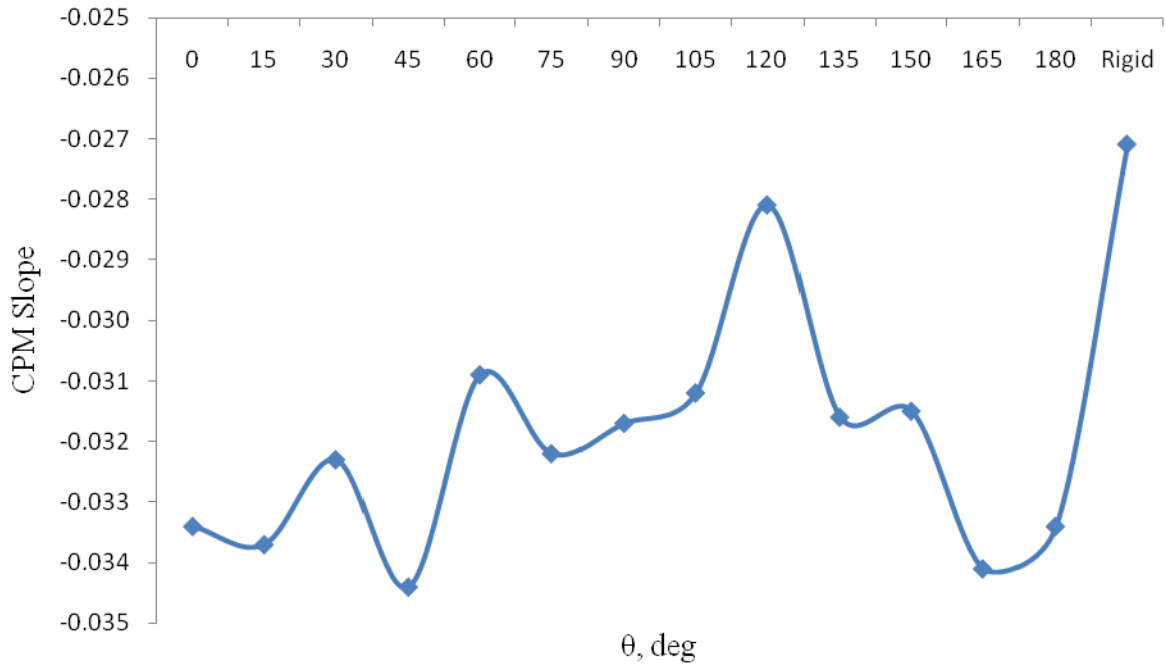


Figure 3-34. Pitching moment slope for crinkled membrane versus crinkle angle at 15 m/s.

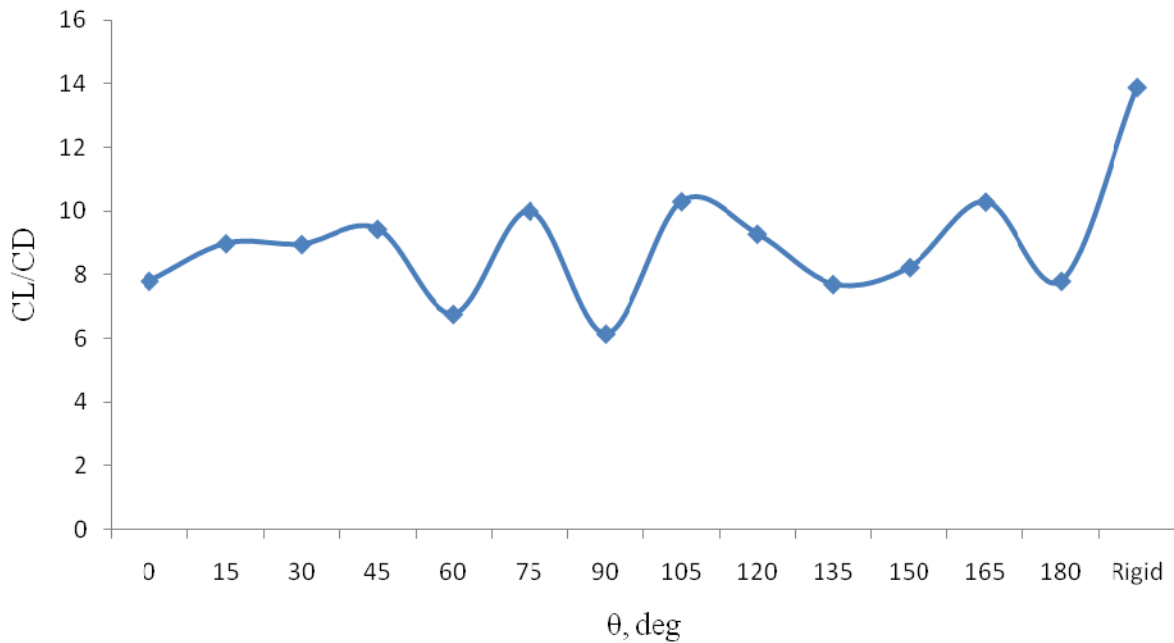


Figure 3-35. Lift over drag ratio versus crinkle angle at  $\alpha=6^\circ$  and 15 m/s.

Maximum lift over drag ratio was achieved at approximately  $6^\circ$  angle of attack for most configurations while for crinkle angles of  $60^\circ$  and  $120^\circ$  this angle corresponds close to  $4^\circ$  (Figure 3-33); also, for these two angles pitching moments slope values were the highest (Figure 3-34). The reasons of CL/CD and pitching moment slope variations between the different trials are not clear. For instance, looking at Figure 3-35 at crinkle angles of  $75^\circ$  and  $105^\circ$  high and similar lift over drag ratios are seen, and at the crinkle angle of  $90^\circ$  a very significant lower ratio is observed, which cannot be explained only by analyzing the data from VIC; in other words, a direct relationship between the load test and VIC images cannot be made. Other parameters, such as surface effects, the geometry of deformations (area, volume), or a number of unknowns could be affecting the data.

### **3.2.2 Test for Surface Effects**

To understand the nature of the data, a quick test was conducted to seek the effects of the surface, which was to block the air to prevent deformation on the anisotropic silicone membrane. To avoid the membrane to be vacuumed by the lower pressure on the upper surface, the entire bottom area of silicone membrane was glued on the circular carbon-fiber plate (Figure 3-20B). The new specimen was rotated every  $45^\circ$  at 15 m/s with an angle of attack array of  $0^\circ$ - $30^\circ$ ; hence, the data was analyzed for four different configurations.

The silicone rubber acts very similar to brakes causing an immense amount of drag on the wing in comparison to the smooth surfaced rigid wing (Figure 3-36); however, the lift curves are similar to the rigid wing. Rotation of crinkles had very little affect on the lift over drag plot when compared to the differences observed in Figure 3-33; thus, the surface effects can be assumed negligible, particularly looking at the curves for crinkle angles of  $45^\circ$  and  $135^\circ$  that match perfectly. Therefore, the curves seen in Figure 3-33 could not have been caused by surface effects.

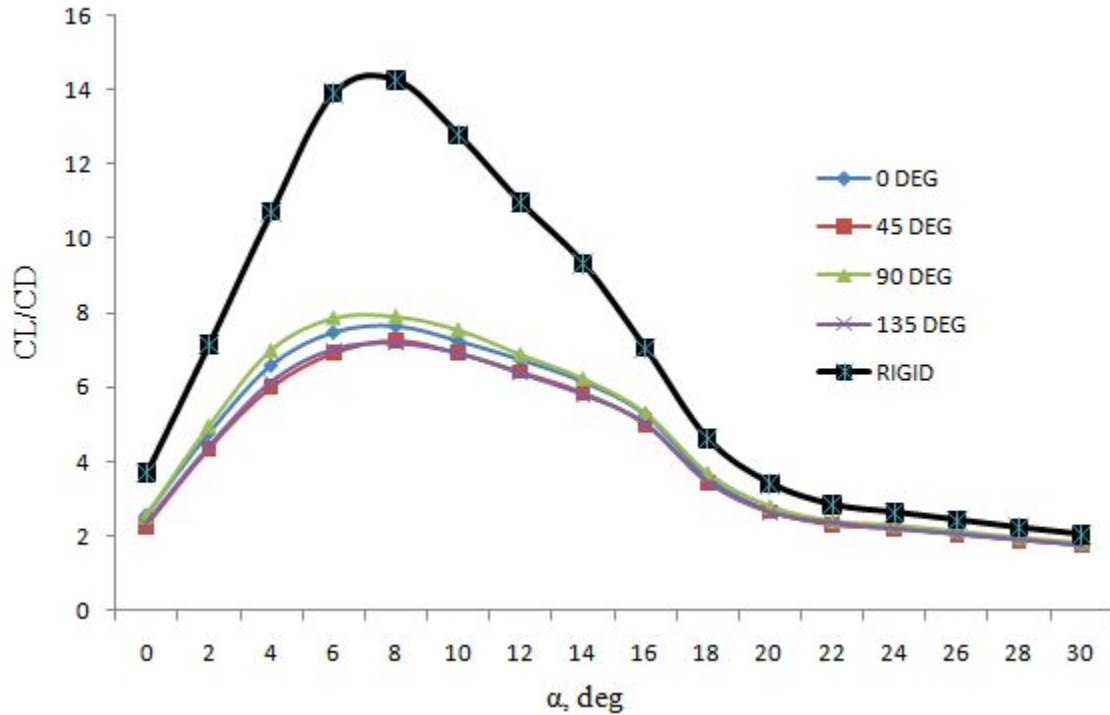


Figure 3-36. Lift over drag ratio curve tested at 15 m/s for four different crinkle angles with the specimen shown in Figure 3-20B.

### 3.2.3 Test for Geometrical Effects

The test bed constructed for this work is not necessarily intended to imitate the exact geometrical deformations that occurred during the crinkled membrane test, but to seek an answer to how much difference would the orientation of an exaggerated geometrical deformation would make, such as the highly eccentric ellipse that was carved on a carbon-fiber plate shown in Figure 3-20C. Basically, the objective of this experiment is similar to simulate the deformations that were observed in the VIC testing and then relate it to the earlier results.

Initially, the minor axis angle,  $\gamma$ , was set equal to zero; then the angle was increased 45° for every trial creating four different configurations (Figure 3-22). Each test was conducted at 15 m/s with an angle of attack array of 0°-30°.

A drastic difference between the lift over drag curves is observed (Figure 3-37); however, the same order of magnitude could not have been expected from the crinkle membrane experiment since the geometrical deformations were entirely different for every crinkle angle. Discussion of why one minor axis angle provides better performance than another is beyond the scope of this test though flow visualization would give an idea about the different drag curves. The objective of the test reached its target by proving that the orientation of the geometric shape matters while it has no effect on the lift curves as expected since the surface area is the same for all configurations.

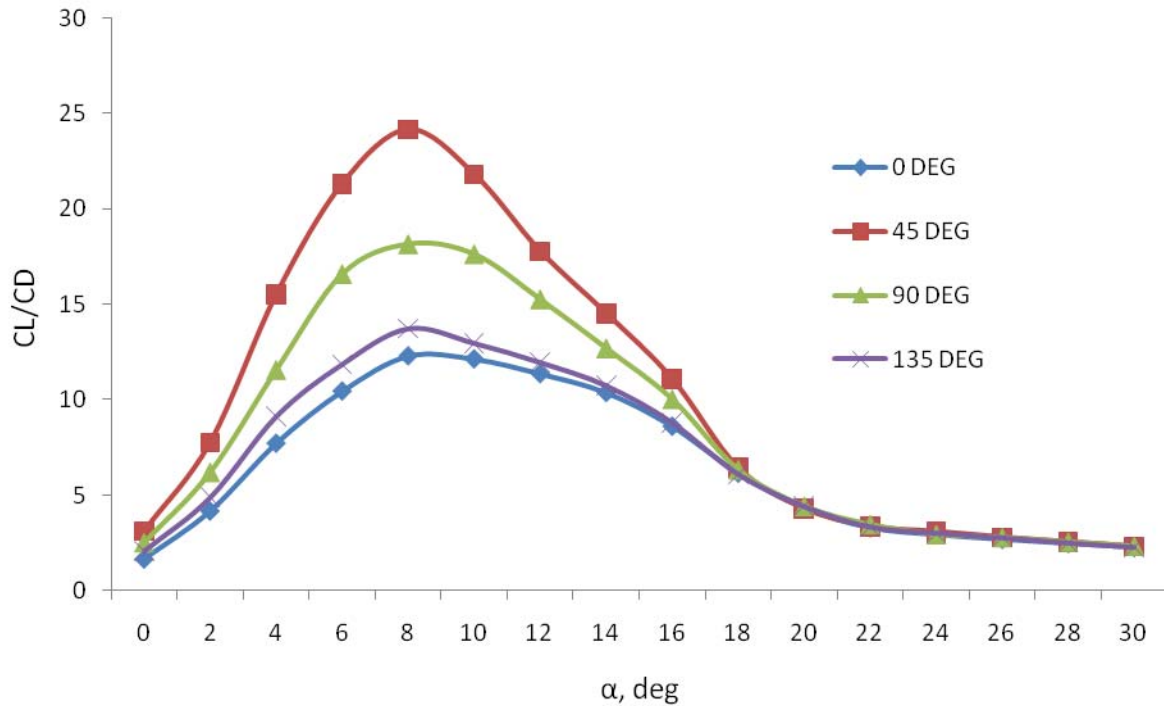


Figure 3-37. Lift over drag ratio curves at four different minor axis angles at 15 m/s.

## CHAPTER 4 CONCLUSIONS AND FUTURE WORK

This work has detailed a series of experimental wind tunnel tests aimed at obtaining a relationship between structural makeup and aerodynamic performance for fixed flexible micro air vehicle wings.

The first wing structure is predicated by a thin latex rubber skin, with stiffer batten structures imbedded within. The battens are designed to washout along the trailing edge in response to an aerodynamic load, meant to alleviate the flight loads: decreased lift slope, delayed stall, etc. Extensive testing of nine disparate membrane/batten structures and one rigid wing for a wide range of (relatively low) Reynolds numbers reveals a significantly more complex relationship:

- 1) Extremely thin battens can provide a substantial trailing edge washout, with peak twist at 50% of the semi-span. Conversely, thicker battens are unable to alleviate these flight loads through twist, and show a sizeable spanwise bending whose severity increases with batten thickness and dynamic pressure. Perhaps due to the bending motion, these wings also tend to adaptively wash-in, for some cases.
- 2) Wings with thin battens alleviate flight loads as the speed increases: delayed stall, shallow lift slopes.
- 3) Wings with thicker battens can augment the flight loads (from the aforementioned wash-in as well as cambering via membrane inflation), and may show extremely large values of lift at high angles of attack: stall is delayed, but pre-stall lift is not drastically reduced.
- 4) A positive spanwise stiffness gradient (thicker at the tip) produces a similar, though muted, result. The wing's aeroelastic response is particularly sensitive to the stiffness of the batten at the wing tip.
- 5) Increasing the distance between battens leads to a sustained vibration along the membrane's trailing edge once a critical dynamic pressure is crossed. This generally decreases the pre-stall lift, but for some cases, shows higher post-stall lift spikes. Scalloping the trailing edge removes the vibration, and, at lower speeds, can recover some of the pre-stall lift.

The second wing structure is configured by embedding three various specimens at different angles to seek the effect on aerodynamic performance: one specimen was an anisotropic membrane glued onto a carbon-fiber ring, the second was the same membrane glued onto the

surface of a carbon-fiber plate, and the third was an isotropic silicone membrane glued on a carbon-fiber plate that had an elliptical shape carved in. An inclusive testing of a total twenty wing configurations yielded the following results:

- 1) Changing the crinkle angle on the first specimen had an effect on the lift over drag ratio data while the lift curves for different orientations remained unchanged.
- 2) VIC testing clarified some of the unknowns to why the crinkle angle affects the drag curves.
- 3) Utilizing the second specimen at different configurations showed surface effects had no influence on the lift over drag plots; also, this experiment has shown that using silicone membrane increases the drag.
- 4) Changing the orientation of the geometrical deformation on the wing have proven an immense effect on the drastic changes observed in the first specimen results.

Future work will utilize various flow visualization techniques to obtain further understanding of the unresolved issues evident in the above results. Specifically, the underlying physics behind the drastically reduced stalling behavior shown by some of the wing structures, as well as the role wing tip vortices play in the aeroelastic behavior, particularly at higher angles of attack, where a close interaction with the longitudinal flow separation seems likely.

APPENDIX  
EXTRA VISUAL IMAGE CORELATION IMAGES

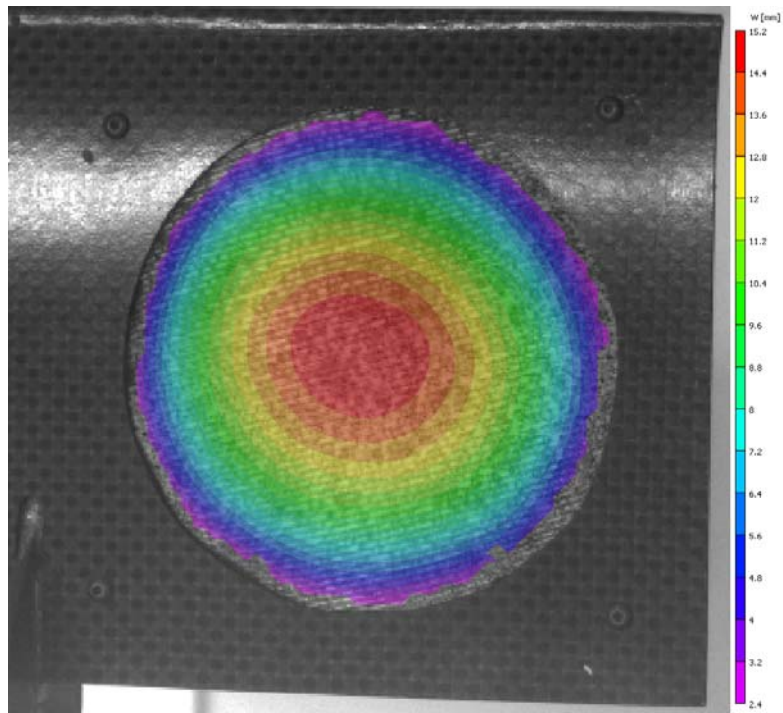


Figure A-1. Deformation on the right side of the wing at  $\theta=105^\circ$  and  $\alpha=10^\circ$ .

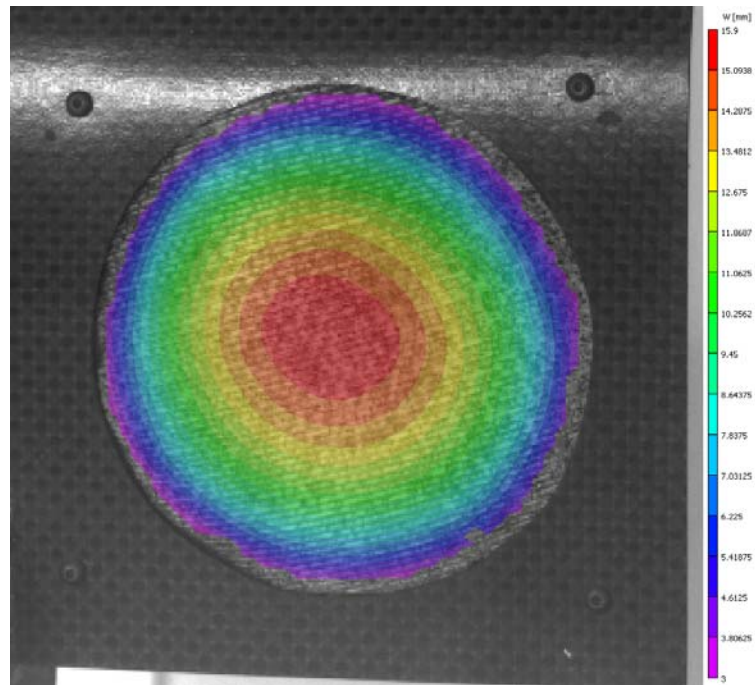


Figure A-2. Deformation on the right side of the wing at  $\theta=105^\circ$  and  $\alpha=15^\circ$ .

## REFERENCES

- [1] Pisano, W., Lawrence, D., "Autonomous Gust Insensitive Aircraft," AIAA Guidance, Navigation, and Control Conference, Honolulu, HI, August 18-21, 2008.
- [2] Kajiwar, I., Haftka, R., "Simultaneous Optimal Design of Shape and Control System for Micro Air Vehicles," AIAA Structures, Structural Dynamics, and Materials Conference, St. Louis, MO, April 12-15, 1999.
- [3] Stanford, B., Ifju, P., Albertani, R., Shyy, W., "Fixed Membrane Wings for Micro Air Vehicles: Experimental Characterization, Numerical Modeling, and Tailoring," *Progress in Aerospace Sciences*, Vol. 44, No. 4, pp. 258-294, 2008.
- [4] Stanford, B., Ifju, P., "Aeroelastic Topology Optimization of Membrane Structures for Micro Air Vehicles," *Structural and Multidisciplinary Optimization*, DOI: 10.1007/s00158-008-0292-x.
- [5] Gad-el-Hak, M., "Micro-Air-Vehicles: Can They be Controlled Better?" *Journal of Aircraft*, Vol. 38, No. 3, pp. 419-429, 2001.
- [6] Mueller, T., "The Influence of Laminar Separation and Transition on Low Reynolds Number Airfoil Hysteresis," *Journal of Aircraft*, Vol. 22, No. 9, pp. 763-770, 1985.
- [7] Lin, J., Pauley, L., "Low-Reynolds-Number Separation on an Airfoil," *AIAA Journal*, Vol. 34, No. 8, pp. 1570-1577, 1996.
- [8] Tang, J., Zhu, K., "Numerical and Experimental Study of Flow Structure of Low-Aspect Ratio Wing," *Journal of Aircraft*, Vol. 41, No. 5, pp. 1196-1201, 2004.
- [9] Young, A., Horton, H., "Some Results of Investigation of Separation Bubbles," *AGARD Conference Proceedings*, No. 4, pp. 779-811, 1966.
- [10] Song, A., Tian, X., Israeli, E., Galvao, R., Bishop, K., Swartz, S., Breuer, K., "Aeromechanics of Membrane Wings with Implications for Animal Flight," *AIAA Journal*, Vol. 46, No. 8, pp. 2096-2106, 2008.
- [11] Fleming, G., Bartram, S., Waszak, M., Jenkins, L., "Projection Moiré Interferometry Measurements of Micro Air Vehicle Wings," *SPIE Paper* 4448-16.
- [12] Wu, P., Stanford, B., Ifju, P., "Structural Deformation Measurements of Anisotropic Flexible Flapping Wings for Micro Air Vehicles," *AIAA Structures, Structural Dynamics, and Materials Conference*, Schaumburg, IL, April 7-10, 2008.
- [13] Hu, H., Tamai, M., Murphy, J., "Flexible-Membrane Airfoils at Low Reynolds Numbers," *Journal of Aircraft*, Vol. 45, No. 5, pp. 1767-1778, 2008.

- [14] Rojratsirikul, P., Wang, Z., Gursul, I., “Unsteady Aerodynamics of Membrane Airfoils,” AIAA Aerospace Sciences Meeting and Exhibit, Reno, NV, January 7-10, 2008.
- [15] Mastramico, N., Hubner, P., “A Study of Wake Characteristics for Membrane Flat and Cambered Plates,” AIAA Aerodynamic Measurement Technology and Ground Testing Conference, Seattle, WA, June 23-26, 2008.
- [16] Sutton, M., Cheng, M., Peters, W., Chao, Y., McNeill, S., “Application of an Optimized Digital Correlation Method to Planar Analysis,” *Image and Vision Computing*, Vol. 4, No.3, pp. 143-151, 1986.
- [17] Schreier, H., Braasch, J., Sutton, M., “Systematic Errors in Digital Image Correlation Caused by Intensity Interpolation,” *Optical Engineering*, Vol. 39, No. 11, pp. 2915-2921, 2000.
- [18] Fitt, A., Pope, M., “The Unsteady Motion of Two-Dimensional Flags With Bending Stiffness,” *Journal of Engineering Mechanics*, Vol. 40, No. 3, pp. 227-248, 2001.
- [19] Albertani, R., Stanford, B., Hubner, J., Ifju, P., “Aerodynamic Coefficients and Deformation Measurements on Flexible Micro Air Vehicle Wings,” *Experimental Mechanics*, Vol. 47, No. 5, pp. 625-635, 2007.
- [20] Carmichael, B., “Low Reynolds Number Airfoil Survey,” NASA Contractor Report, CR 165803, 1981.
- [21] Katz, J., Plotkin, A., *Low-Speed Aerodynamics*, Cambridge University Press, Cambridge, UK, 2001.
- [22] Waszak, M., Jenkins, N., Ifju, P., “Stability and Control Properties of an Aeroelastic Fixed Wing Micro Aerial Vehicle,” AIAA Atmospheric Flight Mechanics Conference and Exhibit, Montreal, Canada, August 6-9, 2001.
- [23] Birch, J., Dickinson, M., “Spanwise Flow and the Attachment of the Leading-Edge Vortex on Insect Wings,” *Nature*, Vol. 412, pp. 729-733, 2001.
- [24] Ormiston, R., “Theoretical and Experimental Aerodynamics of the Sailwing,” *Journal of Aircraft*, Vol. 8, No. 2, pp. 77-84, 1971.
- [25] Munday, D., Jacob, J., “Active Control of Separation on a Wing with Oscillating Chamber,” *Journal of Aircraft*, Vol. 39, No. 1, pp. 187-189, 2002.
- [26] Stanford, B., Ifju, P., “An Anisotropic Elastomer Membrane” University of Florida, FL, August, 2008.
- [27] Post Daniel, Han Bongae, and Ifju Peter. “Production of Silicone Submasters.” *High Sensitivity Moire*. New York: Springer-Verlag, 1994. 432-434.

## BIOGRAPHICAL SKETCH

Yaakov Jack Abudaram was born in Istanbul, Turkey in 1981. As a curious child would fall apart every single little car or toy he had instead of playing with them. Throughout all of his life, he was very much into building model ships, airplanes, and buildings. Having been under the influence of his father he had always wanted to become a medical doctor; though, during the last year of high school realizing he could not stay away from numbers, he chose to study a major that would fulfill his desire: he studied physics for two years at the University of Kocaeli in Izmit, Turkey. Afterward, took the opportunity to come to the United States, then learn English, and continue on his education at a community college aiming to study aerospace engineering at the University of Florida. He earned his dual Bachelor of Science Degree in Mechanical and Aerospace Engineering. During the last two semesters of his college years his enthusiasm toward airplanes pushed him to the doors of Micro Air Vehicle Laboratory. After working there for a few weeks, he felt like this laboratory was where he belonged to having seen the opportunity to combine his interest of building models with academia. He spent extensive hours at the lab building wings and fuselages, installing servos, linkages, motors, cameras, and talking to his supervisor, Kyuho Lee, about airplanes and life. Finally, he found himself studying under Dr. Peter Ifju as a graduate student, and now he has come to one of the crossroads of his life by having written a thesis and looking for a job in the industry. He wants to get a PhD in the future, but only if it is possible to do so under Dr. Peter Ifju at the Micro Air Vehicle Laboratory.